

---

# PULSED LASER DEPOSITION OF THIN FILMS

---

Edited By

Douglas B. Chrisey

and

Graham K. Hubler

Naval Research Laboratory, Washington, D.C.



A WILEY-INTERSCIENCE PUBLICATION

**JOHN WILEY & SONS, INC.**

New York • Chichester • Brisbane • Toronto • Singapore

- Arunava Gupta**, T. J. Watson Research Center, IBM Research Division, Yorktown Heights, New York 10598
- Kolagani S. Harshavardhan**, Neocera, Inc., 335 Paint Branch Drive, College Park, Maryland 20742
- James S. Horwitz**, Naval Research Laboratory, Code 6670, 4555 Overlook Avenue, S.W., Washington, D.C. 20375
- Graham K. Hubler**, Naval Research Laboratory, Code 6670, 4555 Overlook Avenue, S.W., Washington, D.C. 20375
- Roger Kelly**, Dipartimento di Fisica, Università Degli Studio di Trento, Povo (Trento), Italy
- Jacque C. S. Kools**, Philips Research Laboratories, Eindhoven, The Netherlands
- Robert E. Leuchtner**, Department of Physics, University of New Hampshire, Durham, New Hampshire 03824
- Qi Li**, Department of Physics, Center for Superconductivity, University of Maryland, College Park, Maryland 20742
- Simeon Metev**, Bias, Bremer Institut für Angewandte, Strahltechnik N, Klagenfurter Strasse, Bremen, Germany
- Antonio Miotello**, Dipartimento di Fisica, Università Degli Studio di Trento, Povo (Trento), Italy
- Ross E. Muenchausen**, Los Alamos National Laboratory, Los Alamos, New Mexico 87545
- Satish B. Ogale**, Department of Physics, University of Poona, Pune, India
- Alberto Piqué**, Neocera, Inc., 335 Paint Branch Drive, College Park, Maryland 20742
- Kathy L. Saenger**, T. J. Watson Research Center, IBM Research Division, Yorktown Heights, New York 10598
- James A. Sprague**, Naval Research Laboratory, Code 6670, 4555 Overlook Avenue, S.W., Washington, D.C. 20375
- Thirumalai Venkatesan**, Department of Electrical Engineering and Physics, Center for Superconducting Research, University of Maryland, College Park, Maryland 20742
- Xin Di Wu**, Los Alamos National Laboratory, Los Alamos, New Mexico 87545
- Xiao Xing Xi**, U.S. Department of Commerce, National Institute of Science and Technology, Gaithersburg, Maryland 20899-0001
- Jeffrey S. Zabinski**, U.S. Air Force, WRDC/MLBT, Wright-Patterson Air Force Base, Dayton, Ohio 45424

## CONTENTS

Preface	xxiii
List of Acronyms	xxv

### 1. History and Fundamentals of Pulsed Laser Deposition

<i>Jeffery T. Cheung</i>	
1.1 Introduction	1
1.2 The History of Pulsed Laser Deposition: A Chronological Overview	5
1.2.1 1960–1969	6
1.2.2 1970–1979	7
1.2.3 1980–1987	8
1.2.4 1987–Present	10
1.3 History of Theoretical Development	11
1.4 History of Improvement in Experimental Techniques: Reduction of “Splashing”	13
1.4.1 Origin of Splashing	14
1.4.2 Solutions to Avoid Splashing	15
1.5 Deposition with Continuous Wave Lasers	18
References	19

### 2. Equipment

*Steven M. Green, Alberto Piqué, Kolagan S. Harshavardhan,  
and Jeffrey Bernstein*

2.1 Introduction	23
2.2 Lasers	24
2.2.1 Excimer Basics	25
2.2.2 Excimer Discharge Design	27
2.2.3 Beam Characteristics	29
2.2.4 Gas Mixtures	32
	ix

2.3 Optics	34
2.3.1 Lenses and Apertures	35
2.3.2 Mirrors	36
2.3.3 Beam Splitters	37
2.3.4 Laser Windows	38
2.4 Deposition Systems	38
2.4.1 Chambers	40
2.4.2 Target Manipulation	42
2.4.3 Substrate Holders and Heaters	43
2.4.4 Pumps, Gas Flow, and Vacuum Gauges	46
2.4.5 Particle Filters	48
2.5 Safety	49
2.6 Facilities	50
2.7 Suppliers	53
References	54
<b>3. Mechanisms of Pulsed Laser Sputtering</b>	
<i>Roger Kelly and Antonio Miotello</i>	
3.1 Introduction	55
3.2 Description of the Primary Mechanisms	58
3.2.1 Collisional Sputtering	60
3.2.2 Thermal Sputtering	63
3.2.3 Electronic Sputtering	65
3.2.4 Exfoliational Sputtering	67
3.2.5 Hydrodynamic Sputtering	69
3.3 Description of the Secondary Mechanisms	72
3.3.1 Definitions	72
3.3.2 Outflow with Reflection	77
3.3.3 Effusion with Reflection	79
3.3.4 Effusion with Recondensation	81
3.4 Final Comments	83
References	85

#### 4. Surface Modification of Materials by Cumulative Laser Irradiation

*Stephen R. Foltyn*

4.1 Introduction	89
4.2 Thermal Response of the Target to a Laser Pulse	89
4.3 Low-fluence Irradiation: Laser-Induced Periodic Surface Structures	90
4.4 Irradiation at PLD Fluence Levels: Cone Formation	93
4.4.1 Attributes of Laser Cones	94
4.4.2 Cone-Formation Mechanisms	98
4.5 Effects of Surface Modification on Pulsed Laser Deposition	103
4.5.1 Film Composition	103
4.5.2 Film-Deposition Rate	104
4.5.3 Vaporization from Voids	107
4.6 Secondary Effects of Surface Modification	108
4.6.1 Translational Energy Distributions	108
4.6.2 Particulates	108
4.6.3 Plume Direction/Distribution	109
4.6.4 Target Coupling	109
4.7 Avoiding Surface Modification	110
4.7.1 Irradiation Geometry	110
Acknowledgments	111
References	111

#### 5. Diagnostics and Characteristics of Laser-Produced Plasmas

*David B. Geohegan*

5.1 Introduction	115
5.2 General Features of Laser Plasmas and their Characterization	117
5.3 Diagnostic Techniques	119
5.3.1 Mass Spectroscopy	119
5.3.2 Ion Probes	124
5.3.3 Optical Spectroscopy	128
5.3.4 Laser-Induced Fluorescence	141
5.3.5 Photography and Imaging	144

5.4 Background Gas Effects	144
5.5 Clusters and Particulates	157
5.6 Conclusions	161
Acknowledgments	162
References	162
<b>6. Particulates Generated By Pulsed Laser Ablation</b>	
<i>Li-Chyong Chen</i>	
6.1 Introduction	167
6.2 Particulates Characterization	168
6.2.1 Velocity	169
6.2.2 Chemistry	170
6.2.3 Microstructure	176
6.2.4 Spatial Distribution	177
6.3 Effects of Processing Parameters	178
6.3.1 Laser Fluence	180
6.3.2 Laser Wavelength	182
6.3.3 Ambient Gas Pressure	184
6.3.4 Target-to-Substrate Distance	188
6.3.5 Other Parameters	188
6.4 Elimination of Particulates	189
6.4.1 Mechanical Approaches	190
6.4.2 Deposition Geometry	192
6.4.3 Other Techniques	193
6.5 Applications of Particulates	193
6.5.1 Composites	194
6.5.2 Nanophases	195
6.6 Summary	195
Acknowledgments	196
References	196
<b>7. Angular Distribution of Ablated Material</b>	
<i>Kathy L. Saenger</i>	
7.1 Introduction	199

7.2 Measurements Methods	200
7.2.1 General Considerations	200
7.2.2 Film-Based Methods	201
7.2.3 Probe-Based Methods	202
7.3 Survey of Experimental Findings	202
7.3.1 Plume Orientation	203
7.3.2 Angular Distribution: Influence of Target Topography	207
7.3.3 Angular Distribution: Influence of Target-Substrate Distance	208
7.3.4 Angular Distribution: Influence of Laser Spot Dimensions	209
7.3.5 Angular Distribution: Influence of Laser Parameters	209
7.3.6 Ambient Gas Effects	211
7.3.7 Angular Dependence of Film and Plume Composition	212
7.4 Models	213
7.4.1 Derivation of the Cosine-Power ( $\cos^p \theta$ ) Distribution	214
7.4.2 Numerical Models: Assumptions, Results, and Predictions	218
7.4.3 Explanations for 2-Component and Fluence-Independent Angular Distributions	221
7.4.4 Models for Composition Nonuniformity	222
7.5 Summary/Conclusions	224
References	225
<b>8. Film Nucleation and Film Growth in Pulsed Laser Deposition of Ceramics</b>	
<i>James S. Horwitz and James A. Sprague</i>	
8.1 Introduction	229
8.2 Film Nucleation and Growth	231
8.2.1 Volmer-Weber Nucleation and Growth	234
8.2.2 Frank-van der Merve Nucleation and Growth	234
8.2.3 Stranski-Krastinov Nucleation and Growth	235
8.2.4 Effects of Substrate Surface Microstructure	235
8.2.5 Expected Effects of Pulsed Laser Deposition Conditions	236
8.3 Postdeposition Microscopy of YBCO	238

8.3.1 Relationship of Electrical Transport to Microstructure	238
8.3.2 Relationship of Microstructure to Nucleation	239
8.3.3 Scanning Electron Microscopy	239
8.3.4 Transmission Electron Microscopy	244
8.3.5 Scanning Tunneling Microscopy and Atomic Force Microscopy	246
8.4 In Situ Diagnostics of YBCO Film Growth	250
8.5 Conclusions and Future Directions	252
References	253
<b>9. Processes Characteristics and Film Properties in Pulsed Laser Plasma Deposition</b>	
<i>Simeon Metev</i>	
9.1 Introduction	255
9.2 Deposition Characteristics	255
9.2.1 Plasma Parameters	255
9.2.2 Film Growth Mode	257
9.3 Influence of the Deposition Characteristics on the Film Properties	260
9.3.1 Influence of the Plasma Parameters	260
9.3.2 Influence of the Film Growth Mode	262
9.4 Conclusion	263
References	264
<b>10. Novel Pulsed Laser Deposition Approaches</b>	
<i>Arunava Gupta</i>	
10.1 Introduction	265
10.2 Deposition in the Presence of a Background Gas	266
10.3 Deposition in the Presence of a Separate Source of Neutral Atomic Species	271
10.4 Plasma and Ion Beam-Assisted Deposition	273
10.4.1 Plasma-Assisted Deposition	274
10.4.2 Ion Beam-Assisted Deposition	279

10.5 Laser Irradiation and Heating of Substrate During Deposition	281
10.6 Dual-Beam Laser Ablation	285
10.7 Concluding Remarks	287
References	288
<b>11. Commercial Scale-Up of Pulsed Laser Deposition</b>	
<i>James A. Greer</i>	
11.1 Introduction	293
11.2 Large-Area PLD Approaches	294
11.3 Comparison of Large-Area PLD Approaches	296
11.4 Large-Area PLD Requirements	299
11.4.1 Target Utilization and Resurfacing	299
11.4.2 Window Purging	300
11.4.3 Large-Area Substrate Heating	300
11.4.4 Laser Requirements, Deposition Rate, and Rate Monitoring	301
11.4.5 Vacuum Requirements	304
11.4.6 Large-Area Particulate Reductions Schemes	304
11.4.7 Large-Area Multilayer Films	305
11.4.8 Other Aspects of Large-Area PLD	306
11.5 PLD on Nonplanar Surfaces	306
11.6 Future Trends in Large-Area PLD	309
References	311
<b>12. Pulsed Laser Deposition: Future Trends</b>	
<i>T. Venkatesan</i>	
12.1 Introduction	313
12.2 Intrinsic Advantages of PLD	313
12.3 Materials Trend	314
12.4 Impact of PLD on Thin-Film Deposition Facilities	316
12.5 Scale-up to Large Areas	316
12.6 Elimination of Particles	317

12.7	Deposition Rate and Layer-by-Layer Control	319
12.8	In Situ Deposition, Processing, and Analysis Facility	320
12.9	Enhancements and Accessories	320
12.10	Reduction in Film Crystallization Temperatures	321
12.11	Conclusion	322
	References	322
<b>13.</b>	<b>Comparison of Vacuum Deposition Techniques</b>	
	<i>Graham K. Hubler</i>	
13.1	Introduction	327
13.2	Deposition Techniques	328
13.3	Morphological Development of Films: Temperature Effects	330
13.3.1	Initial Stages of Film Growth	330
13.3.2	Thick-Film Development	332
13.4	Morphological Development: Energy Effects	334
13.4.1	Molecular-Dynamics Simulation	335
13.4.2	Ion Mixing and Thermodynamic Bias	336
13.4.3	Displacement Damage Calculations	337
13.4.4	Energetic Flux: Background-Gas Synergy	340
13.5	Effect of Arrival Rate	341
13.5.1	Kinetic Limitations	341
13.6	Vacuum Quality	342
13.6.1	Summary	344
13.7	Comparison of Techniques	344
13.7.1	Fundamental Deposition Criteria	344
13.7.2	Practical Deposition Criteria	349
13.7.3	Comparison of Materials Deposited with the Techniques	351
13.8	PLD in Perspective	353
	Acknowledgments	354
	References	354

#### 14. Pulsed Laser Deposition of High-Temperature Superconducting Thin Films for Active and Passive Device Applications

*Ross E. Muenchausen and Xin Di Wu*

14.1	Introduction	357
14.2	Active Devices	358
14.2.1	SNS Junctions	358
14.2.2	SIS Junctions and Three-Terminal Devices	367
14.2.3	Bolometers	368
14.3	Passive Devices	370
14.3.1	Filters, Resonators, and Delay Lines	370
14.3.2	Kinetic Inductance Devices	373
14.3.3	Multi-Chip Modules	374
14.4	Future Directions	376
	Acknowledgments	376
	References	377

#### 15. Field Effects in High- $T_c$ Superconducting Thin Films

*Xiao Xing Xi*

15.1	Introduction	381
15.2	Field-Effect Device Structure	382
15.3	Electric Field Modulation of Basic Physical Properties	384
15.4	Prospects for High- $T_c$ SuFET Devices	388
15.5	Conclusion	391
	References	392

#### 16. Epitaxial Oxides on Semiconductors

*David K. Fork*

16.1	Introduction	393
16.2	General Remarks	395
16.3	Oxides on Silicon	399
16.3.1	Epitaxial Silicon-on-Insulator Structures	401
16.3.2	Epitaxial Oxides as Buffer Layers on Silicon	401

16.4	Epitaxial Oxides on GaAs	407
16.5	Summary	412
	Acknowledgments	412
	References	412
<b>17.</b>	<b>Noncrystalline Carbon Films with the Bonding and Properties of Diamond</b>	
	<i>Carl B. Collins and Farzin Davanloo</i>	
17.1	Introduction	417
17.2	Laser Ablation as a High Fluence Source of Ions	418
17.3	Interfacial Growth	421
17.4	Energetic Condensation of Carbon Ions	423
17.5	Applications of Noncrystalline Films with the Properties of Diamond	425
17.6	Conclusions	428
	References	429
<b>18.</b>	<b>Tribological Coatings</b>	
	<i>Michael S. Donley and Jeffrey S. Zabinski</i>	
18.1	Introduction	431
18.2	Background: Tribological Materials	432
18.3	Experimental Apparatus	433
18.4	PLD Tribological Coatings	434
	18.4.1 Lubricant Coatings	434
	18.4.2 Hard Coatings	441
18.5	Future Directions	448
18.6	Summary	450
	References	450
<b>19.</b>	<b>Pulsed Laser Deposition of Metals</b>	
	<i>Jacque C. S. Kools</i>	
19.1	Introduction	455

19.2	Specific Aspects of PLD of Metals	456
	19.2.1 Laser Ablation of Metals	456
	19.2.2 Targets	457
	19.2.3 Droplets	457
	19.2.4 Requirements for a Deposition Machine	459
19.3	Some Examples of PLD of Metals	460
	19.3.1 In Situ Contact Metallization	460
	19.3.2 Magnetic Materials	462
	19.3.3 Nonequilibrium Alloys	463
	19.3.4 Metallic Multilayers	463
19.4	Conclusions	469
	Acknowledgments	469
	References	469
<b>20.</b>	<b>Ferroelectrics</b>	
	<i>Robert E. Leuchtner and Kenneth S. Grabowski</i>	
20.1	Introduction	473
20.2	Laser-Deposited Ferroelectric Materials	475
20.3	Optimized Deposition Conditions	477
	20.3.1 Composition: Volatile Constituents	478
	20.3.2 Crystal Structure and Orientation	482
	20.3.3 Morphology and Uniformity	483
	20.3.4 Electrical Properties	493
20.4	Applications	495
	20.4.1 Nonvolatile Random-Access Memory	495
	20.4.2 Novel Microelectronic Devices	498
	20.4.3 Sensors and Actuators	500
	20.4.4 Smart Materials and Adaptive Structures	501
20.5	Future Directions	501
20.6	Concluding Remarks	502
	Acknowledgments	503
	References	503

**21. Pulsed Laser Deposition of Ferrite Thin Films***Carmine A. Carosella and Douglas B. Chrisey*

21.1	Introduction	509
21.2	Applications of Ferrite Thin Films	511
21.3	Other Approaches to Fabricating Ferrite Thin Films	513
21.4	Ferrite Thin Films Made by Pulsed Laser Deposition	513
21.5	Future Directions for the PLD of Ferrites	516
	References	517

**22. Bandgap Engineering of HgCdTe by Pulsed Laser Deposition***Jeffrey T. Cheung*

22.1	Introduction	519
22.2	Experimental Approach	520
22.3	Results	525
22.3.1	Single Barriers	525
22.3.2	Superlattices	527
22.3.3	Optical Properties	529
22.4	Conclusion	532
	Acknowledgments	532
	References	532

**23. Pulsed Laser Deposition Applied to High  $T_c$  Ultrathin Films and Superlattices***Qi Li*

23.1	Introduction	535
23.2	Substrate and Sample Preparation	536
23.2.1	Substrate	536
23.2.2	Deposition of Ultrathin Films and Superlattices	537
23.3	Ultrathin YBCO Films	539
23.4	$\text{YBa}_2\text{Cu}_3\text{O}_{7-\delta}/(\text{Pr}_x\text{Y}_{1-x})\text{Ba}_2\text{Cu}_3\text{O}_{7-\delta}$ Superlattices	541
23.4.1	Superconducting Transition	541
23.4.2	Critical Current Anisotropy	544

23.5	Conclusion	546
	Acknowledgment	547
	References	547

**24. Pulsed Laser Deposition of Biocompatible Thin Films***Catherine M. Cotell*

24.1	Introduction	549
24.2	Requirements for PLD of Hydroxylapatite and Other Calcium Phosphate Phases	551
24.3	Deposition of Pure, Crystalline HA	552
24.4	Control of Calcium Phosphate Phase and Chemical Composition	553
24.5	Microstructure and Surface Morphology of PLD Calcium Phosphate Films	559
24.6	Mechanisms of Ablation of HA Targets	560
24.7	Adhesion of PLD HA Films to Substrates	562
24.8	Osteoblast Cell Response to PLD-HA Films	564
24.9	Conclusions and Projections for the Future of PLD of Biomaterials	565
	Acknowledgments	566
	References	566

**25. Deposition of Polymer Films by Laser Ablation***Satish B. Ogale*

25.1	Introduction	567
25.2	Current State of Knowledge	568
25.3	Deposition of Polyphenylene Sulphide Polymer by Pulse Laser Ablation	570
25.4	Synthesis of Polymer-Metal Composite Thin Films by Pulsed Laser Coablation	573
25.5	Applicability of Laser-Deposited Polymer Films	576
25.6	Summary	578
	Acknowledgment	578



References	578
------------	-----

# Appendix: Bibliography of Films Deposited by Pulsed Laser Deposition

Kathy L. Saenger

Table A.1. Overview of Thin Film Materials Deposited by PLD	582
--	-----

References	590
------------	-----

Index	605
-------	-----

## PREFACE

This book grew from a series of articles on pulsed laser deposition of thin films published in the February 1992, issue of the *Materials Research Society Bulletin*. Dave Nagel of the Naval Research Laboratory pointed out to us the opportunity to amplify these articles into a book that highlights this unique new deposition technique and captures the excitement those of us feel that work in the field.

Interest in pulsed laser deposition (PLD) as a technique to deposit thin films of complex materials is growing exponentially. The success PLD has had in the deposition of a wide variety of materials has spurred activity worldwide. The reasons for this explosion of research activity is that virtually any material, from pure elements to multicomponent compounds (up to six-element compounds) can be deposited; the stoichiometry of the charge material is faithfully reproduced in the film; in situ deposition of oxide materials without the need for postdeposition processing is straightforward; and perhaps most of all, the technique is simple and the capital cost is low.

It may be anticipated that the number of researchers joining the effort will multiply in the coming years, as it becomes apparent to others that the PLD process represents a breakthrough in materials processing. Currently, there are no books about PLD available (only three conference proceedings), in part because the field is so new that the power of the technique is only now becoming apparent. We felt that the field would be well served by a comprehensive book covering all phases of PLD relevant to deposition of thin films: a reference book for those already in the field, a teaching document for those wishing to join and a complete overview of what is required to set up and begin research in pulsed laser deposition and understand the basic principals of the process.

The book contains 25 chapters by as many internationally recognized experts in their fields covering a broad range of topics in pulsed laser deposition of thin films. It does not cover some related areas, for example, desorption induced by electronic transitions (DIET) or laser-induced fusion. The volume is structured into two parts: part one contains 13 up-to-date chapters covering both the fundamental and practical aspects of the technique. It includes the history of PLD (Chapter 1), details of the physics of laser-target interactions (Chapter 4), development of the laser-plume and gas-plume dynamics (Chapters 3, 5, 6, 7), and film formation (Chapters 8, 9, 13), and couples these fundamentals to practical considerations of laser selection and chamber design (Chapter 2), industrial scale up of the PLD process (Chapter

- Schafer, D., B. Brauns, R. Wolf, B. Steiger, and G. Zscherpe (1990), *Vac* 41(4-6), 1084-1086.
- Shettal, R. N., and I. V. Cherbakov (1981), *Crystal Res. Tech* 16(8), 887-891.
- Schwartz, H., and A. J. Demaria (1962), Nat. Electro. Conf. Proc., McCormick Place, Chicago, Ill., XVII 351-365.
- Schwartz, H., and H. A. Tourtellotte (1969), *J. Vac. Sci. Technol.* 6(3), 373-378.
- Smith, H. M., and A. F. Turner (1965), *Appl. Opt.* 4, 147-148.
- Tang, S. P., N. G. Utterback, and J. F. Friichtenicht (1976), *J. Chem. Phys.* 64(9), 3833-3839.
- Von Allmen, M. (1976), *J. Appl. Phys.* 47(12), 5460-5463.
- Wagal, S. S., E. M. Juengerman, and C. B. Collins (1988), *Appl. Phys. Lett.* 53(3), 187-188.
- White, R. M. (1963) *J. Appl. Phys.* 34, 3559.
- Wong, K. H., et al. (1991), *J. Mater. Sci. Lett.* 10, 801-803.
- Wong, K. H., S. K. Hau, P. W. Chau, L. K. Leung, C. L. Choy, and M. K. Wong (1991), *J. Mater. Sci. Lett.* 10, 801-803.
- Wu, X. D., et al. (1990), *Mater. Res. Soc. Symp. Proc.* 191, 129-140.
- Zeitsev-Zatov, S. V., R. A. Martynyuk, and E. A. Protasov (1983), *Sov. Phys. Solid State* 25, 100-103.

## CHAPTER 2

# EQUIPMENT

STEVEN M. GREEN, A. PIQUÉ, and K. S. HARSHAVARDHAN

Neocera, Inc.  
College Park, Maryland

J. S. BERNSTEIN  
Lambda Physik, Inc.  
Acton, Massachusetts

## 2.1 INTRODUCTION

In this chapter we introduce the basic equipment that is required to begin work in pulsed laser deposition (PLD). As presented in the previous and remaining chapters, PLD is an extremely versatile technique for preparing a wide range of thin films and multilayer structures. One of its great advantages, and certainly one of the reasons for its ready acceptance among materials scientists, is the attractive start-up cost of PLD research. The cost advantage is especially striking when one considers that PLD systems can produce films with quality comparable to molecular beam epitaxy (MBE) systems that cost 10 times as much, and more!

Another advantage of PLD, in terms of both ease of use and cost, resides in the fact that the energy source that creates the plume of ejecta, the laser, is *independent* from the deposition system. Thus, complex multilayer films are straightforward to produce within a single system by moving various targets into and out of the beam focal point. And, by using mirrors to change the beam path, several deposition systems can be clustered around a single laser to create an entire deposition laboratory.

Great strides have been made in recent years to bring reliable and user-friendly excimer lasers to the commercial market, a topic covered in depth in the pages that follow. The second topic discusses what optics will be needed between the laser and deposition system. Basic deposition system considerations are presented in the third section. Safety issues and facility requirements associated with operating a PLD laboratory are also discussed in the sections that follow. Lastly, a partial list of suppliers is given at the end of the chapter (Table 2.4).

## 2.2 LASERS

This section provides information on commercially available laser equipment that is commonly used for PLD research. Some fundamentals of the lasers, operating characteristics, and various configurations are discussed.

In general, the useful range of laser wavelengths for thin-film growth by PLD lies between 200 nm and 400 nm. Most materials used for deposition work exhibit strong absorption in this spectral region. Absorption coefficients tend to increase as one moves to the short wavelength end of this range and the penetration depths into the target materials are correspondingly reduced. This is a favorable situation because thinner layers of the target surface are ablated as one moves closer to the 200-nm mark. The stronger absorption at the short wavelengths also results in a decrease in ablation fluence thresholds. Below 200 nm, strong absorption by the Schumann–Runge bands of molecular oxygen can make working in this part of the spectrum difficult. The optics are also more difficult. Bulk damage due to color center formation occurs much easier at the shorter ultraviolet (UV) laser wavelengths. Within the 200-nm to 400-nm range there are few commercially available laser sources capable of easily delivering the high-energy densities ( $>1 \text{ J/cm}^2$ ), in relatively large areas ( $10 \text{ mm}^2$  or larger), that are required for laser deposition work.

Most of the work accomplished to date has been centered around excimer and  $\text{Nd}^{3+}$ :YAG lasers as the deposition source (see the bibliography by K. L. Saenger at the end of this book).  $\text{Nd}^{3+}$ :YAG lasers are solid-state systems. The neodymium ions serve as the active medium and are present as impurities in the YAG (yttrium aluminum garnet) host. The neodymium ions are pumped optically into their upper states by flashlamps. High output energies are achieved by using two YAG rods in an oscillator/amplifier configuration. Q-switching allows this configuration to produce outputs up to 2 J/pulse. At these high energies pulse repetition rates are limited to 30 Hz. A good discussion of YAG lasers and Q-switched operation can be found in Yariv (1976).

The fundamental laser emission of  $\text{Nd}^{3+}$ :YAG occurs at 1064 nm, well outside the desired range indicated earlier. Using a nonlinear crystal, the 1064-nm output can be frequency doubled with about 50% power conversion efficiency yielding an output at 532 nm. In order to produce light in the UV, the 532-nm output is mixed with the residual 1064-nm light or frequency doubled again. The resulting outputs at 355 nm or 266 nm are produced with the respective efficiencies of  $\sim 20\%$  and  $\sim 15\%$  relative to the fundamental.

The excimer is a gas laser system. Unlike  $\text{Nd}^{3+}$ :YAG lasers, excimer lasers emit their radiation directly in the UV. High outputs delivering in excess of 1 J/pulse are commercially available. These systems can also achieve pulse repetition rates up to several hundred hertz with energies near 500 mJ/pulse. Consequently, the excimer is generally the laser of choice for PLD work.

Table 2.1 gives a list of excimer wavelengths that have been developed into

TABLE 2.1 Excimer Laser Operating Wavelengths

Excimer	Wavelength (nm)
$\text{F}_2$	157
ArF	193
KrCl	222
KrF	248
XeCl	308
XeF	351

commercial laser systems. The corresponding active excimer molecule is indicated as well. Of the excimers listed, KrF and XeCl have been extensively used for PLD. KrF is the highest gain system for electrically discharged pumped excimer lasers and is the popular choice among the PLD community. Although KrCl operates at a shorter wavelength than KrF, it is a low-gain system and does not output the pulse energies required for PLD work. A more detailed discussion of excimer lasers is given below.

### 2.2.1 Excimer Basics

The light output from an excimer laser is derived from a molecular gain medium in which the lasing action takes place between a bound upper electronic state and a repulsive or weakly bound ground electronic state. Because the ground state is repulsive, the excimer molecule can dissociate rapidly (on the order of a vibrational period  $\sim 10^{-13} \text{ s}$ ) as it emits a photon during transition from upper state to ground state. The high ratio of upper state lifetime to lower state lifetime makes the excimer, in a sense, the perfect laser medium because population inversion and therefore high gain are so easily achieved. Figure 2.1 shows a typical molecular potential energy diagram of an excimer system.

The excimer molecules are formed in a gaseous mixture of their component gases, such as Xe, HCl, and Ne in the case of the XeCl laser. Energy is pumped into the gas mixture through avalanche electric discharge excitation. The pumping creates ionic and electronically excited species that react chemically and produce the excimer molecules. Electron-beam excitation and microwave discharge excitation have also been used as a means to pump the gas mixture. Commercially available laser systems producing several hundred millijoules/pulse are all of the electric discharge type.

The details of the kinetics and chemical reactions leading to the formation of the excimer molecules are quite complex and can consist of many steps. Some of the more important reactions for the case of KrF are listed below

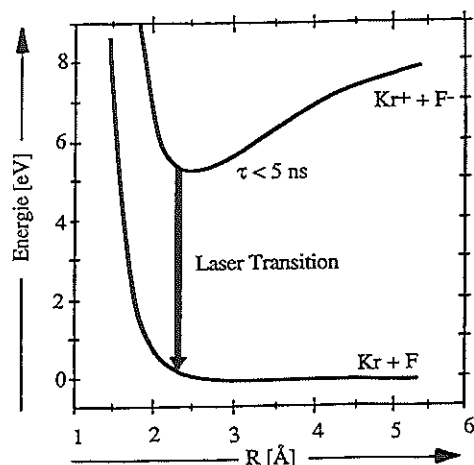
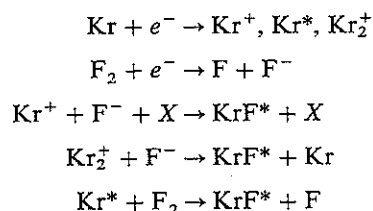


Figure 2.1. Schematic diagram of the electronic potential of the KrF excimer.

where the \* denotes an electronically excited species and X denotes a third body (He, Ne).



Once the excimer is formed, it will decay via spontaneous emission and collisional deactivation giving the molecule a lifetime of  $\sim 2.5$  ns. Moderate output energies of several hundred millijoules per laser pulse dictate an excimer population density requirement on the order of  $10^{15}/\text{cm}^3$ . Therefore, in order for lasing action to occur, the formation rate of the ionic and excited precursors must be fast enough to produce excimers at a rate of several  $10^{23}/\text{cm}^3/\text{s}$ .

As discussed before, the gas mixture is pumped by a fast avalanche electric discharge. In order to achieve the preceding formation rate, the discharge must meet certain requirements. Because the excimer is stabilized by a third body, the fast kinetics involved in producing the excimers require total gas pressures in the range of 2 to 4 atmospheres within the discharge volume. Other discharge parameters are electron densities on the order of  $10^{15}/\text{cm}^3$ , current densities of  $10^3 \text{ A}/\text{cm}^2$ , and electron temperatures of approximately 1200 K. These requirements are met with electric discharge field strengths of 10–15 kV/cm. Consequently, discharge electrode spacings are limited to 2–3 cm.

Hence, the discharge voltages can be in the range of 20–45 kV. Larger electrode spacing can provide higher laser output energies, but the resulting voltages are too large and troublesome. At these higher voltages discharge instabilities are more severe and corona discharge between high-voltage electrical components becomes problematic. Hence, the technology and engineering involved in designing an appropriate discharge is quite important. Some aspects of electric discharge design are discussed below.

## 2.2.2 Excimer Discharge Design

The basic avalanche electric discharge circuit consists of some capacitors, inductor coils, and a pair of electrodes. A typical layout of an early electric discharge design is shown in Figure 2.2. The discharge requirements just discussed necessitate peak powers of  $10^8$ – $10^9 \text{ W}$  delivered to the discharge region (20–40 J deposited in 20–50 ns). Typically, the following events occur. The storage capacitors are charged to at most 40 kV. The thyatron switch is fired and the energy is then transferred to the peaking capacitors over a time of approximately 100 ns. When the peaking capacitors become sufficiently charged, the energy is transferred to the discharge region with a time duration of 20–50 ns. As one can easily see, the electrical requirements are extremely demanding on the high-voltage circuit components.

These early discharge designs suffer from short component lifetime and poor reliability. The main failure component of these early designs is the high-voltage thyatron switch. With these designs, the thyatron has to withstand voltages up to 40 kV, currents as high as 15 kA, and current rates  $dI/dt > 10^{11} \text{ A/s}$ . In order to meet these demands, thyatrons have to be used in the less than optimum “grounded grid” configuration. Consequently, thyatron lifetime is limited to a mere  $10^7$  discharges.

A schematic of state-of-the-art discharge design currently used in some commercial excimer lasers is shown in Figure 2.3. This design eliminates the

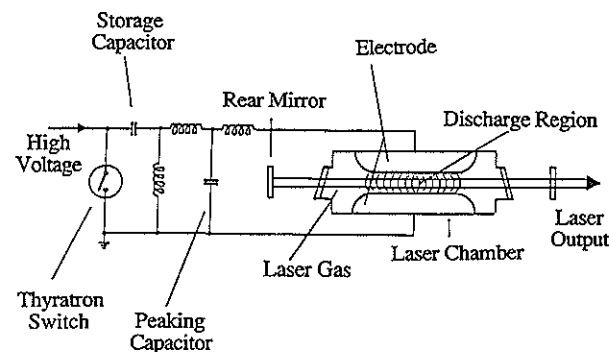
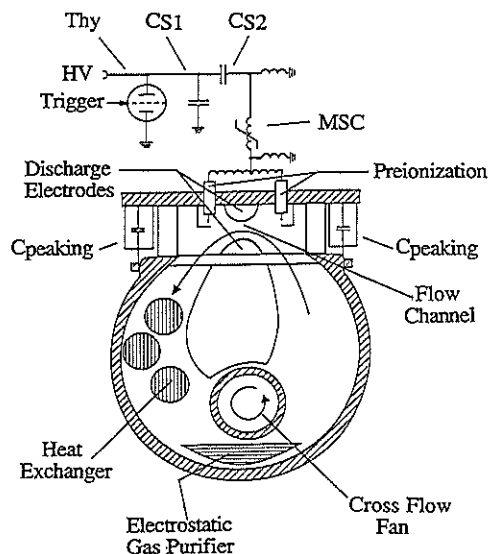


Figure 2.2. Schematic diagram depicting an early excimer laser discharge circuit design.



**Figure 2.3.** Diagram illustrating MSC discharge circuitry with cross-sectional view of excimer laser tube.

flaws associated with the early designs. The main technological feature is the magnetic-switch-control (MSC) switch. The MSC addresses the problem of short component lifetime suffered by earlier discharge designs. With MSC technology, the very fast time constants required of the discharge are decoupled from the thyatron. As a result, the current rate through the thyatron ( $di/dt$ ) as well as peak thyatron current are substantially reduced.

The circuit also allows the thyatron hold-off voltage to be reduced by as much as 50%. Hence, the thyatron is used in the normal "grounded cathode" configuration. Because the MSC effectively reduces the switching load on the thyatron, smaller, less expensive thyatrons can be used. This is good news for excimer users since replacement costs for large thyatrons can be quite substantial.

A magnetic switch is an inductor that can change state from an unsaturated condition, with large inductance, to a saturated condition with low inductance. A properly designed switch, such as the MSC, will allow this change of state to occur very rapidly and with minimal power losses. With such a design, the circuit in Figure 2.3 can be viewed as two independent circuits. The thyatron circuit can have its own characteristic inductance independent of the low inductance discharge. Hence, storage capacitor  $C_{s1}$  can discharge with a long time constant and therefore reduce the peak current and  $di/dt$  experienced by the thyatron.

$C_{s2}$  also discharges except its current is used to saturate the MSC. The

circuit is designed so that saturation is coincident with  $C_{s1}$  polarity reversal. The effective voltage applied to the discharge electrodes is double that which was applied to the storage capacitors. Since approximately 40 kV is needed for the discharge, only 20 kV has to be switched by the thyatron. The stored energy (from  $C_{s1}$  and  $C_{s2}$ ) passes through the saturated MSC and is transferred to  $C_{peaking}$ . The peaking capacitors serve to peak up the current pulse and create the fast discharge. An added plus with the design in Figure 2.3 is that while the MSC is saturated, current conducts only in one direction. Thus, any reverse current (which can be detrimental to thyatrons) generated by the discharge is blocked by the MSC. MSC technology has been around for nearly 10 years. It is a proven technology that has extended thyatron lifetimes by as much as two orders of magnitude. Typically, on the order of  $10^9$  discharges for a given thyatron can be realized.

For more detailed information on thyatrons and magnetic switches, see Basting et al. (1984).

### 2.2.3 Beam Characteristics

A homogeneous uniform laser output is required for good-quality deposition work. Hot spots and deviations from uniformity should be avoided as much as possible. This is especially important when working with multicomponent deposition targets. Poor beam quality can result in nonstoichiometric films as well as undesirable droplet formation.

The quality of an excimer laser beam is intimately coupled to the discharge. Obtaining a high-quality uniform output begins with a homogeneous breakdown of the laser gas. To ensure this situation results, the gas is preionized (see Figure 2.3) just prior to the full-blown discharge. Preionization creates electrons by partially ionizing the gas mixture with UV light and thus providing an initial electron density in the gas mixture.

The UV light is generated from spark gaps (preionization pins) that run along the length of the electrodes. This method of preionization is very robust and practically all commercially available electric discharge excimer lasers use this technology. Because the UV light is strongly absorbed by the laser gas, the penetration depth of the UV photons is limited. This puts some practical limitations on the cross-sectional dimensions for a uniform homogeneous output beam.

Preionization using X-rays is an alternative method to spark gaps. X-ray preionization results in larger beam cross sections and increased beam uniformity due to an increased penetration depth by the X-rays. With X-ray preionization, a separate power supply is required to power the X-ray tubes. A separate high-voltage switch (thyatron) and high-voltage circuitry are also required to fire the tubes. Hence, the expense of the X-ray preionized laser may outweigh its advantages in most laser deposition applications, except perhaps where large-area ablation is essential.

Another major factor affecting the output beam characteristics are the

discharge electrodes. The electrode construction, in terms of its geometry and material composition, is the main factor determining the spatial distribution of the laser output. The electrical properties of excimer gases are an important part of the discharge circuit and must be considered when designing the electrode shape. Such considerations will lead to an efficient discharge with a uniform laser output. Because the different excimer gases can have very different electrical properties, electrode shapes can be optimized. Larger beam cross sections with increased uniformity and higher output energies are possible with optimized electrodes. Because shape is so important, precise machining of the electrodes is essential. Materials that lend themselves to these requirements must be chosen.

Figures 2.4A and 2.5A display three-dimensional beam profiles of two Lambda Physik LPX 300 KrF lasers. In Figure 2.4A, the laser is equipped with a set of standard "multigas electrodes." These electrodes are designed (in terms of shape and material construction) for operation on any of the excimer wavelengths. The laser output in Figure 2.5A is obtained from a laser with "fluorine-optimized" electrodes. A laser equipped with this electrode configuration can only be operated with KrF or ArF gas mixtures. In both cases, the output energy is asymmetrically distributed. The output energy distribution is

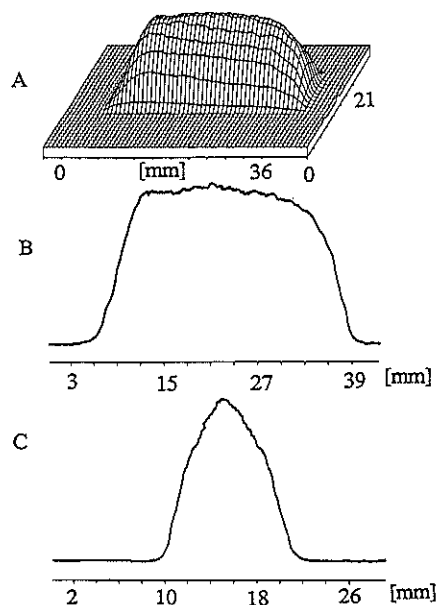


**Figure 2.4.** Beam profiles obtained from a Lambda Physik LPX 300 KrF laser with multigas electrodes. (A) Three-dimensional beam profile. (B) Horizontal cross section. (C) Vertical cross section.

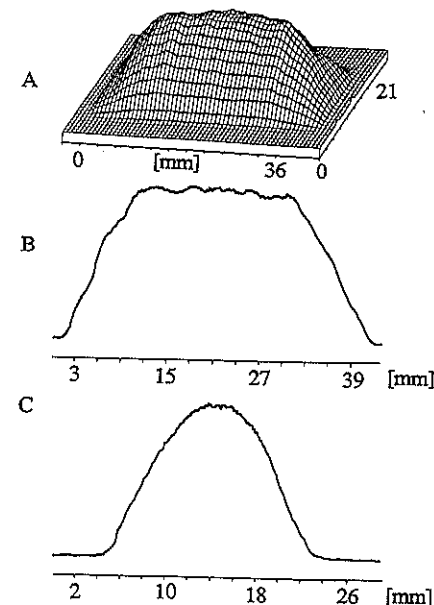


**Figure 2.5.** Beam profiles obtained from a Lambda Physik LPX 300 KrF laser with fluorine-optimized electrodes. (A) Three-dimensional beam profile. (B) Horizontal cross section. (C) Vertical cross section.

best described as nearly "top hat" along the horizontal axis (see Figures 2.4B and 2.5B) and near-Gaussian along the vertical axis (see Figures 2.4C and 2.5C). The top-hat distribution corresponds to the axis connecting the anode and cathode.

The profiles in Figures 2.4 and 2.5 show typical output characteristics for excimer lasers and are due both to the electric field distribution in the discharge and the optical design of the resonator. It can be seen from the cross-sectional graphs in Figures 2.4 and 2.5 that the fluorine-optimized electrodes lead to a larger area beam with increased uniformity. Consequently, more energy can be extracted from the discharge. In the case of KrF, an increase in output energy of approximately 30% (or more) can be expected when the laser tube is configured with fluorine-optimized electrodes.

In addition to the asymmetrical energy distribution, the divergence of the excimer laser is also radially asymmetric. The divergence in the long axis is typically three times greater than in the short axis. Typical divergence values are 4.5 mrad and 1.5 mrad for the long and short axes, respectively. Since the lasers are usually placed in somewhat close proximity to the deposition chambers, the asymmetric divergence and the somewhat large divergence angles are generally of little consequence for PLD applications. On the other hand, if it is required for a specific application, radial symmetry of the

divergence as well as reduced divergence angles can easily be obtained. This is done by exchanging the normal or stable resonator optics (flat high reflector and flat output coupler) with a set of unstable resonator optics (convex high reflector and meniscus lens output coupler). In addition to reducing the divergence to 0.4 mrad and making a symmetrically diverging beam, the output beam profile arising from the unstable resonator is symmetric as well. The down side, however, is that the output energy is only 60% of that achieved with the stable resonator design.

The electrodes and preionization pins of all electric discharged pumped excimers will erode with use and form impurities in the gas mixture. Over time this erosion or burnoff will lead to a deterioration of the beam quality. The uniformity of the output beam as well as the shot-to-shot amplitude stability can be affected. Formation of "streamers" in the output beam is a typical characteristic that can occur due to degrading electrodes. Streamers are striations or streaks visually observed in the laser output. They are caused by arcing between specific sites on the discharge electrodes. The arcing can take place between sites on a single electrode (anode or cathode), between electrode and preionization pins, or between anode and cathode. When arcing becomes severe, the output energy will fluctuate wildly and the laser may not be able to sustain operation. In this case, the laser must be refurbished with new electrodes and preionization pins.

In order to resolve these problems and maximize the lifetime of electrodes and preionization pins, the choice of materials for these components is quite important. The choice of materials must also reflect the ability to obtain a beam profile with a high degree of uniformity as discussed earlier. Nickel has been widely used as an electrode material because of its high wear resistance, good electrical properties, and halogen compatibility. Typically, electrodes have been fabricated from solid nickel or nickel clad over an aluminum body. Brass alloys have also been used as an electrode material. Both XeCl and KrF are compatible with nickel but only KrF can be used with the brass alloy construction.

Regardless of the electrode construction, users should expect a usable working lifetime of approximately 1/2 billion shots. Of course, this number depends on the particular gas mixture (i.e. wavelength), quality of gases used, and operating environment. One should keep in mind that the laser beam profile is a dynamic parameter and will change slowly over time according to the condition of the discharge electrodes.

## 2.2.4 Gas Mixtures

The gas mixtures for excimer lasers are comprised of three components: rare gas (Xe, Kr), halogen (HCl or F<sub>2</sub>), and Ne as a buffer gas. Total volume of the laser head can be from 40 to 60 liters, depending on the laser size and desired output energy. Operating pressures are around 3000 mbar and the total volume of gas required is approximately 125–200 liters. A typical gas recipe and

required purity levels are given in Table 2.2 for a laser that operates with KrF. An estimate of yearly gas expense is also given in Table 2.2. This estimate is based on a gas consumption rate of one fill per week. This corresponds to continuous operation at 15 Hz for a 40-hour week and assumes a working gas lifetime of 2 million laser shots.

The gas fills have a finite lifetime due to slow consumption of the halogen component by impurities arising mainly from degradation of the discharge electrodes and preionization pins. This process generates dust particles comprised of halogen salts. Adequate removal of these dust particles is essential for maximum gas lifetimes and long optics cleaning intervals. Some manufacturers incorporate electrostatic gas precipitators into the laser head, which allows for removal of large particulates from the gas fill. Cryogenic gas processors are also available and may be a viable option, depending on the operating mode (e.g., for high repetition rate) of the laser. These devices bleed off a small portion of the gas fill and freeze out the impurities. The clean gas is injected back into the laser head in close proximity to the cavity optics. Purging the optics in this manner serves to increase window cleaning intervals.

Gas lifetimes are dependent upon the particular halogen in use and upon the laser wavelength. Properly engineered lasers have achieved  $>20 \times 10^6$  shots for chlorine operation and  $>5 \times 10^6$  shots for fluorine operation. A factor of 2 to 3 increase in gas lifetime can be expected when a cryogenic gas processor is connected to the laser. Gas lifetimes also depend on the laser wavelength. A decrease in gas lifetimes are observed with a decrease in laser wavelength. This occurs because absorption cross sections of impurities present in the discharge increase with increasing photon energy. Consequently, photochemistry leading to halogen consumption is an important factor concerning gas lifetimes.

Laser gases have traditionally been available as individual components in their own separate gas bottles. Recently, there has been an increase in the use of premix laser gases. Premix gases are mixed according to a specific recipe for a given laser and packaged in a single bottle. There are a number of advantages

TABLE 2.2 Gas Recipe for Lambda Physik Model LPX 200 and Estimated Gas Expense Based on One Fill per Week

KrF Excimer	Purity (%)	Pressure (mbar/fill)	Volume (l/fill)	Expense (\$/l)	Expense (\$/fill)	Expense (\$/year)
5% F <sub>2</sub> in He	99.9	70	5.0	0.68	3.40	176.80
Kr	99.99	150	7.5	3.40	25.50	1326.00
Ne	99.99	2750	112.5	0.16	18.00	936.00
He <sup>a</sup>	99.995					300.00
Total		2950	125.0		46.90	2738.80

<sup>a</sup>A few cylinders of He are needed for flushing purposes.

and trade-offs between operation with premix or separate bottles. Laser manufacturers have responded to the increasing popularity of premix gases by configuring lasers optimized for either premix or separate gas bottle operation.

Premix operation offers the potential for a lower cost operation. In addition, there is considerably less plumbing of gas lines, making the installation process that much easier. With a premix gas delivery, the fraction of halogen component in the gas bottle is already diluted to the same level, approximately 0.2%, as in the laser head. A separate bottle of the halogen component normally contains a mixture of 5% halogen in He. There is an obvious safety advantage when dealing with premix bottles. Additionally, the gas regulator and plumbing lines are under a less corrosive environment with premix operation.

Separate gas bottle operation affords the user flexibility. Some researchers and end users require the ability to periodically change the operating wavelength of the laser. Changing the laser from fluorine operation to chlorine operation and then back is therefore necessary. If the laser is to be operated in such a mode, then separate gas bottle delivery is usually suggested.

Most commercially available excimer lasers in today's market can be energy-stabilized. The stabilization algorithms ramp up the high voltage over time as the halogen is depleted, thus allowing for a constant output energy. When the high voltage reaches a predetermined maximum level, the stabilization routine can call for a small amount of halogen to be injected into the laser head. The high voltage then drops and the process is repeated over again. Hence, algorithms that call for halogen injections can only be used with separate gas bottle delivery systems.

## 2.3 OPTICS

Between the output port of the laser and the laser port of the deposition chamber, optical elements are placed in order to steer and focus the beam. The optical elements that couple the energy from the laser to the target are lenses and apertures; mirrors; beam splitters; and laser windows.

This section begins with the following cautionary note: **KEEP YOUR OPTICS CLEAN!** Fingerprints, dust, smears, and other adherents not only interfere with the beam path, they can cause permanent damage to the optical elements. One of the most common mistakes made by novices in the laboratory is in using dirty lenses, mirrors, and windows. The dirt attenuates the beam, then couples energy into the optical element causing damage. Optics designed for UV wavelengths can be rather delicate, and are usually fairly expensive. Using gloves and an occasional wipe with lens paper, you can prevent damage, and add greater reproducibility to your experiments. Also, as part of routine chamber maintenance, do not forget to clean the deposited material off of the laser port window.

### 2.3.1 Lenses and Apertures

By far, lenses are the most important among the optical elements listed earlier. The primary function of the lens is to collect radiation from a point on the source (laser) and focus it to a corresponding point on the target to achieve the required energy density for ablation. In the pulsed laser deposition of various thin films, one of the most important deposition parameters that controls the film stoichiometry and crystallographic quality is the laser energy density (expressed in joules/square centimeter) incident on the target. In most cases, it has been found that the laser energy density has to be above a minimum threshold value in order to obtain films with the same stoichiometry as the target. Spherical lenses are most widely used in PLD, although cylindrical lenses can also be used. Spherical lenses magnify in two orthogonal planes, and hence a point source is imaged as a point. Cylindrical lenses have magnification only in one plane and can change the height of an image without changing its width, imaging a point source as a line. In PLD, cylindrical lenses can be used to change the shape of the laser beam.

A variety of collimating or focusing lenses of various focal lengths and diameters, and made of various materials, are available from a number of manufacturers. While ordering lenses for PLD, it is necessary to consider the range of wavelengths transmitted by the lens material. Table 2.3 lists some of the lens materials and the transmittance range for which they are suitable. As an example, for pulsed laser deposition using a KrF excimer laser at 248 nm, UV-grade fused-silica lenses are a good and cost-effective choice. When inspecting the lens material, be sure it is free of inclusions and bubbles and mechanical distortions.

In achieving the optimum energy density at the target surface, it is necessary to take into account the two most common lens aberrations: spherical

TABLE 2.3 Transmittance Range for Various Lens and Window Materials

Material	Transmittance Range (nm)
Magnesium fluoride	140–7500
Sapphire	150–5000
Calcium fluoride	150–8000
UV-grade fused silica <sup>a</sup>	190–2500, 2600–4000
Borosilicate crown glass	315–2350
Zinc sulphide	400–12,000
Zinc selenide	550–16,000

<sup>a</sup>UV-grade fused silica absorbs energy in the range 2500–2600 nm.



aberration and coma. In spherical aberration, the bundle of rays parallel and close to the optic axis come to focus at a point different from the bundle of rays parallel and away from the optic axis. Spherical aberration can be reduced by using apertures to attenuate the beam away from the optic axis. Of course, this reduces the total energy delivered to the target.

As an alternative, a planoconvex lens can be used for condensing the beam, with the convex surface toward the laser beam. For optimum performance, the lens should be oriented to divide the refraction as equally as possible between the lens surfaces. If the lens is oriented with the plane surface toward the laser, the beam would pass through the plane surface without refraction, resulting in image degradation.

The second common lens aberration, coma, results in a variation of the lens focal length as a function of distance from the lens axis. Again, an aperture before the lens will mitigate this problem. The lens aberrations can also be minimized by taking care that most of the beam passes through the center of the lens, avoiding the thin edges. It is desirable to have a lens diameter at least 1.5 times the  $1/e^2$  Gaussian laser beam diameter so that 99% of the beam passes through the lens.

### 2.3.2 Mirrors

In a PLD laboratory, the expensive excimer laser can be shared by more than one deposition chamber, making the process very cost effective. The film deposition chamber can be positioned in such a way that the normal to the laser port is parallel to the primary laser beam ( $0^\circ$  mode) or perpendicular to the primary beam ( $90^\circ$  mode). In the latter case, the primary beam is reflected off the primary path using standard laser mirrors, with the laser beam incident at an angle of  $45^\circ$  with respect to the normal to the mirror.

Figure 2.6 displays one possible arrangement of four deposition systems operating off of a single primary beam line. Presumably, the individual systems are used for different purposes, and hence each system maintains a dedicated aperture/lens pair. Please note that the various lenses are located *between* the mirror and chamber. This arrangement is suggested because there is an energy density damage threshold for the mirrors. If, due to space constraints or other considerations, the mirror is placed following the lens, extreme care should be taken to avoid damaging the mirror with a focused beam. In the case of the dual-beam chamber, two sets of mirrors and aperture/lens pairs are used following a beam splitter. Beam splitters are discussed in the next section. The mirrors are moved into or out of the beam path in order to direct the laser energy to the operating chamber. It is advised that beam blocks be placed in front of the laser ports for the chambers that are not in use to prevent accidental entry of stray laser energy.

The mirrors used for PLD are dielectric multilayer mirrors and are designed for a desired reflectance. Many manufacturers offer the laser mirrors for  $45^\circ$  incidence, with the laser beam incident on the coating side. Normally, the

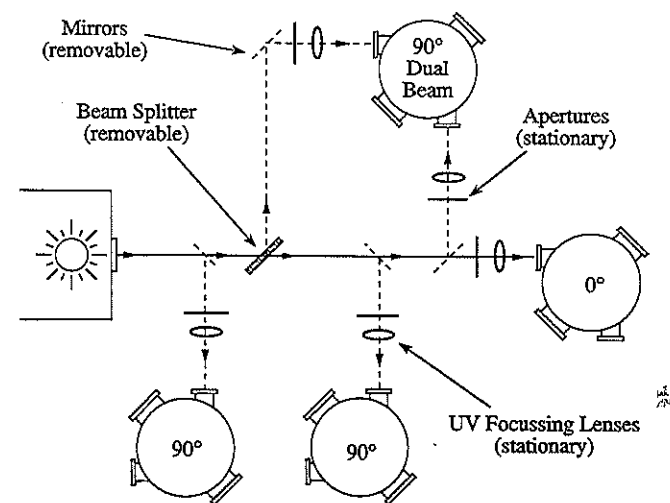


Figure 2.6. An arrangement of four deposition systems and associated optics along a single primary beam path.

dielectric multilayer coatings are optimized for a single wavelength or a very narrow spectral range. These mirrors can contain as many as 13 layers of high index and low index material, each of which is quarter-wave optically thick, deposited on a glass substrate. Such dielectric multilayer mirrors can offer reflectivities up to 99% at the specified wavelength. The reflectance is wavelength dependent; above and below the optimum wavelength, the reflectance is decreased. Extreme care should be exercised in handling these dielectric mirrors, as the coatings are quite delicate.

### 2.3.3 Beam Splitters

Beam splitters split the laser beam into two or more separate beams. Both equal and unequal beam splitting, in terms of energy throughput, are possible depending on the type of beam splitters used. If, for example, the beam were to be sampled for power monitoring (before the beam enters the deposition chamber), only a small amount of beam would be reflected off of the beam splitter, which can be an uncoated glass or fused-silica plate. The transmittance through a fused-silica plate varies with angle of incidence and polarization state of the beam. For less sensitivity to beam angle and polarization changes, one should use an incidence angle less than  $20^\circ$ . The reflectance and transmittance of an uncoated fused-silica-plate beam splitter at  $45^\circ$  is sensitive to variations in the angle of incidence and also the beam polarization.

Another application of a beam splitter is indicated in Figure 2.6. Here, the primary beam is split into two equal-intensity beams that are directed into the

laser ports of a dual-beam chamber with mirrors. Dual-beam PLD is a method used to improve the characteristics of target erosion. For this application, coated-plate beam splitters are used. The coating can be metallic or dielectric. The reflectivity of most thin-film dielectric coatings depends on wavelength, polarization and angle of incidence, so dielectric beam splitters are generally designed for a specific application. Dielectric beam splitters designed for 45° incidence are also available with various reflectance-to-transmittance ratios. As with UV mirrors, an energy density damage threshold exists for coated beam splitters. Please consult the manufacturer's literature for more details.

### 2.3.4 Laser Windows

The laser windows through which the laser enters the deposition chamber should be made out of laser-quality optical material (fused silica for 248 nm), polished to a very high degree of flatness,  $\frac{1}{8}$  to  $\frac{1}{20}$  wave. These windows must be free of defects such as bubbles and inclusions since these defects can deteriorate the beam quality. The various optical materials listed in Table 2.3 can also be used as windows, depending on the wavelength of the excimer laser being used.

## 2.4 DEPOSITION SYSTEMS

Once the laser beam passes through the optical elements, it enters the deposition system. Deposition systems, in general, can become as complex as you wish, combining various deposition methods, such as PLD, magnetron sputtering and molecular beam epitaxy, with load locks, and differential pumping, and analysis equipment, ad infinitum. The purpose of this section is to present the foundation equipment required to produce thin films and multilayers by pulsed laser deposition. A good foundation for a versatile PLD deposition system is comprised of the following elements: chamber, target manipulation, substrate holder and/or heater, pump, gas flow, and vacuum gauging. A particle filter may also be incorporated into system design as an accessory.

Recently, commercial PLD systems and accessories have entered the marketplace. For example, Figure 2.7 displays a complete PLD system available commercially that incorporates the foundation features just described into a portable turnkey unit and Figure 2.7B displays a significantly more elaborate UHV system incorporating load-locks, bellows, manipulators, and so on. Other system configurations are also available (see Table 2.4 at the end of the chapter for a partial list of suppliers). The basic simplicity of PLD has enabled many researchers to design and assemble their own deposition systems, too. If time and resources permit, homebuilt systems may be a cost-effective choice.

The following sections present the various foundation equipment necessary to begin PLD research.

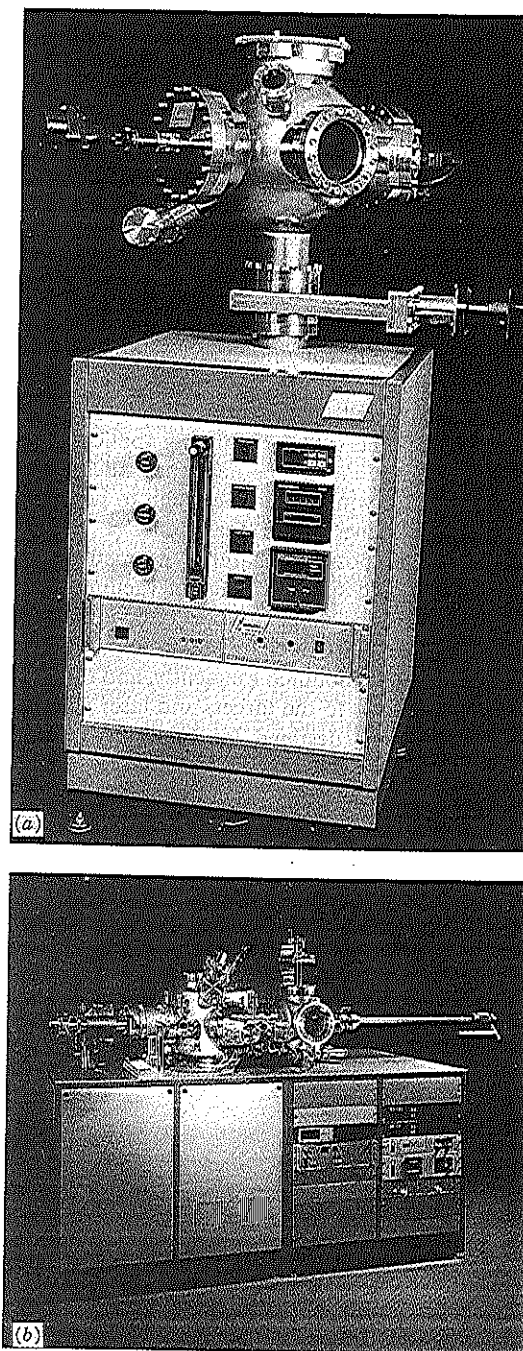


Figure 2.7. Commercially available multilayer deposition systems for PLD produced by (a) Neocera, Inc., and (b) Riber, Inc.

### 2.4.1 Chambers

The deposition chamber is one of the most crucial components in a PLD system. By investing some additional time to think through the various aspects of beam-target-substrate positioning and system maintenance, much setup and operational time and frustration will be saved down the road. The schematic in Figure 2.8 is one example of the many experimental setups that work well, and serves to introduce some of the important parameters to consider when designing a PLD chamber.

In addition to the standard ports required on all vacuum chambers (e.g., pumping port, gas inlet, pressure gauging, and viewports), the PLD chamber must have ports for the targets, substrates, and laser beam. The beam path must be completely unobstructed. In the future, it may be necessary to move the beam focus to different points (i.e., for scanning applications), and therefore plenty of space should be made available near the anticipated beam path. A good idea is to choose a laser window large enough to permit the beam to be focused over several square inches of the focal plane.

There are a multitude of possible chamber geometries to choose from, including crosses, cylinders, and spheres. Users of vacuum equipment tend to develop prejudices based on the shape and feel of equipment they have used in the past. With regard to a PLD chamber, it is wise to remember that targets must be mounted and demounted frequently, and that the laser window must be kept clean. Thus, access to the targets and laser window should be as simple as possible. In systems destined for high throughput or ultrahigh vacuum (UHV) operation, load locking the laser, target, and substrate ports should be considered, although this is generally not necessary for research-and-development systems.

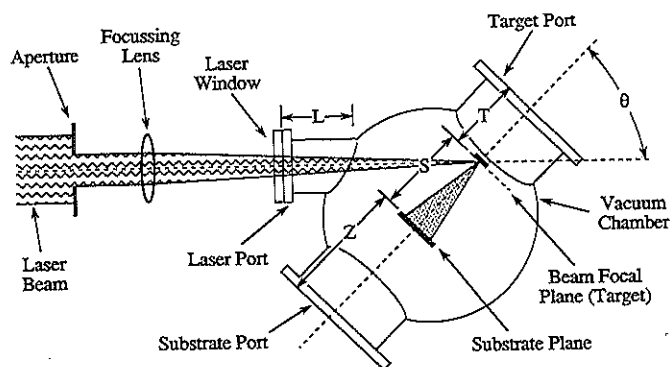


Figure 2.8. Schematic illustration of important parameters to consider when designing a PLD chamber. (Key:  $T$  = target port flange-to-beam focal plane (target) distance;  $Z$  = substrate port flange-to-substrate distance;  $S$  = target-to-substrate distance;  $L$  = laser port length;  $\theta$  = angle between target normal (plume direction) and laser beam.)

If the substrates are to be heated, the chamber will also be heated and may have to be cooled externally. In a well-designed chamber, the heat will be distributed uniformly over the surface, thus minimizing the need for external cooling. Spherical geometries are preferable in terms of uniform heat distribution. A 12-in-diameter sphere with a 300-W heater located near its center will stay fairly cool without any external cooling. (Viewports, on the other hand, may require a cooling fan.) Conversely, a 6-in cross with a 300-W heater will likely require water cooling.

In Figure 2.8, five dimensions are indicated: the laser port length,  $L$ ; the target port flange-to-beam focal plane distance,  $T$ ; the target to substrate distance,  $S$ ; the substrate port flange-to-substrate distance,  $Z$ ; and the angle between the target normal and laser beam,  $\theta$ . When the chamber is manufactured,  $L$ ,  $\theta$ , and  $T + S + Z$  will be fixed, unless additional ports or bellows are included. As usual, there is a trade-off between cost and versatility.

The optimization parameter  $S$ , depends on, among other things, the energy density, chamber pressure, and target morphology. By allowing  $S$  to be adjustable, optimized depositions can be obtained. For most applications,  $S$  will be in the range 3 to 15 cm, although longer distances ( $\sim 20$  cm) could be desirable to increase the surface area which is uniformly coated. In practice, however, the location of the beam focal plane is limited by  $L$ ,  $T$ , and  $\theta$ . Also, unless bellows fixturing is used for the target and substrate ports, the total distance between flanges,  $T + S + Z$ , is fixed. Thus, in order to adjust  $S$ , it is recommended that  $Z$  be an adjustable parameter, as discussed in the section on substrate holders and heaters.

In PLD, the deposition is very forward-directed along the target normal. Considerable material will find its way to all surfaces within the chamber, however, including the laser window, especially when a background gas is employed during the depositions. Material deposited on the window will interact with the laser beam, and the result could be permanent damage to the window. By increasing the length,  $L$ , of the laser port, the rate of material depositing on the window will be reduced. Making  $L$  too long, however, reduces the available area to which the beam may be focused. Thus, a compromise length needs to be chosen that balances these two factors. Also, it is important to clean the window periodically; load locking the laser port should be considered in systems destined for high throughput or UHV operation.

The angle between the laser beam and the beam focal plane needs to be chosen such that the substrate holder and any other fixturing in the chamber will not be in the beam path. Compromises generally need to be made between  $\theta$ ,  $S$ ,  $L$ , and  $T$ , unless significant funds are available for redundant ports and bellows attachments. The angle should not be too small since the size and location of the spot is difficult to control near grazing angles. The angle cannot be too large since, eventually, the substrate holder will get in the way. Angles near  $45^\circ$  are recommended.

Custom chambers and standard PLD chambers can be manufactured by

any one of a number of vacuum equipment distributors (see Table 2.4 at the end of the chapter for a partial list of suppliers). Many of the unforeseen design problems that might be encountered have already been worked out by such specialty companies, which will permit you to concentrate on research questions instead of design questions.

### 2.4.2 Target Manipulation

There are few intrinsic restrictions placed on the targets used in a PLD system. Successful depositions can be made from pressed powders, sintered pellets, cast material, single crystals, and metal foils. The main differences between these different target morphologies is in the nature of the target erosion, and the generation of particulates. A good rule of thumb is that high-density and highly homogeneous targets yield the best films. However, even the best targets must be resurfaced (sanded flat) at regular intervals in order to perform optimally. For this reason, targets should be easily accessed within the chamber, and mounting and demounting should be as simple as possible. The reader is referred to Chapter 4 on surface modification of materials by cumulative excimer laser irradiation by S. Foltyn and Chapter 6 on particulates by L. C. Chen for more detailed discussions of laser-target interactions.

In terms of uniform target erosion and consumption, the most common practice is to rotate the target during deposition. In this fashion, an annular region of a disk-shaped target will be ablated. By imaging a rectangular aperture onto the radius, the target will be consumed with maximum efficiency. An alternative practice is to ablate off the round surface of a cylindrical target. In this case, the target is rotated about the cylinder axis. It is less common to use this arrangement when multilayer depositions are anticipated.

The laser beam may also be scanned over the surface of a flat target to provide for uniform erosion, but this has the disadvantage of moving the plume relative to the substrate. When large substrates are to be coated (significantly larger than 1 cm in diameter), such beam scanning can be used to improve the edge-to-edge thickness and compositional uniformity.

When disk-shaped targets are used, they are generally fixed to a target mount that is slid onto a rotation axle. Two schemes are commonly employed to fix the targets: a clamping mechanism, or bonding. Bonding of the target to the target mount is preferred for several reasons. Targets may get quite hot due to the focused laser beam and also if substrate heaters are employed. By using a silver paste or epoxy, good thermal contact between target and mount can be achieved, alleviating the heating problem. If clamping is chosen, it is usually necessary to provide a water-cooled shroud around the target to minimize target heating. Another advantage of bonding is the ease with which targets can be resurfaced: the target mount can contain a grasping point, reducing the need to directly handle the source material. Also, irregularly shaped targets of various sizes can be bonded to standardized target mounts, increasing the versatility of the deposition system.

One of the great advantages of PLD over other thin-film fabrication techniques is the ease with which in situ multilayer structures can be formed. A target carousel containing several targets is generally employed for this application. Figure 2.9A is a photograph of one such carousel. The schematic in Figure 2.9B provides labels for some of the important portions of the assembly. As a minimum, provision must be made for target rotation or rastering (for uniform erosion) and in situ target exchange (e.g., carousel rotation and indexing). In addition, ease of use dictates that the targets be readily accessible for replacement and resurfacing. Shields might be required to minimize target cross-contamination and to protect the carousel mechanism. Such devices for multilayer depositions are available through the vendors in Table 2.4 at the end of the chapter.

The ease with which multilayers are fabricated can be translated directly into ease of process automation. Most lasers can be triggered by an external pulse. Thus, an algorithm that combines target positioning and laser triggering into a programmed routine is rather straightforward. Automated multilayer deposition accessories are commercially available through Neocera and Kurt J. Lesker (see Figure 2.10).

### 2.4.3 Substrate Holders and Heaters

As with most thin-film deposition techniques, the manner in which the substrate is held and its location and orientation relative to the target are important parameters in a PLD system. Frequently, the substrate must be heated to produce good adhesion and/or epitaxy. For many of the materials commonly deposited by PLD, substrate temperatures in excess of 800°C must be maintained with uniformities better than  $\pm 0.5\%$ . The formation of epitaxial complex metal oxides, such as PLZT and YBCO ( $\text{YBa}_2\text{Cu}_3\text{O}_{7-x}$ ) require oxygen ambients and high temperature.

Since the evaporants are ejected as a highly forward-directed plume of material along the target normal, the substrate must be held directly opposite the target. The optimal target-to-substrate distance,  $S$ , depends on several factors, most significant of which is the energy delivered to the target. Higher beam energies permit larger  $S$ 's to be used. Also, the deposition rate can be controlled by treating  $S$  as a variable. For example, to reduce the deposition rate, one might increase  $S$  rather than reduce the beam energy. The ability to adjust  $S$  is therefore desirable. For more exacting applications, it will be necessary to move the substrate laterally, necessitating  $X$  and  $Y$  motion, too.

When the film is to be deposited on an unheated substrate, only the simplest substrate holder is required. Any device that permits the substrate to be located opposite the target within the chamber will do, such as a simple clamping mechanism. Such mechanisms can frequently be rigged "quick-and-dirty" and provide satisfactory results at little cost.

If the substrate is to be heated to moderate temperatures (below  $\sim 600^\circ\text{C}$ ) in a nonoxidizing atmosphere, the substrate holder becomes only slightly more

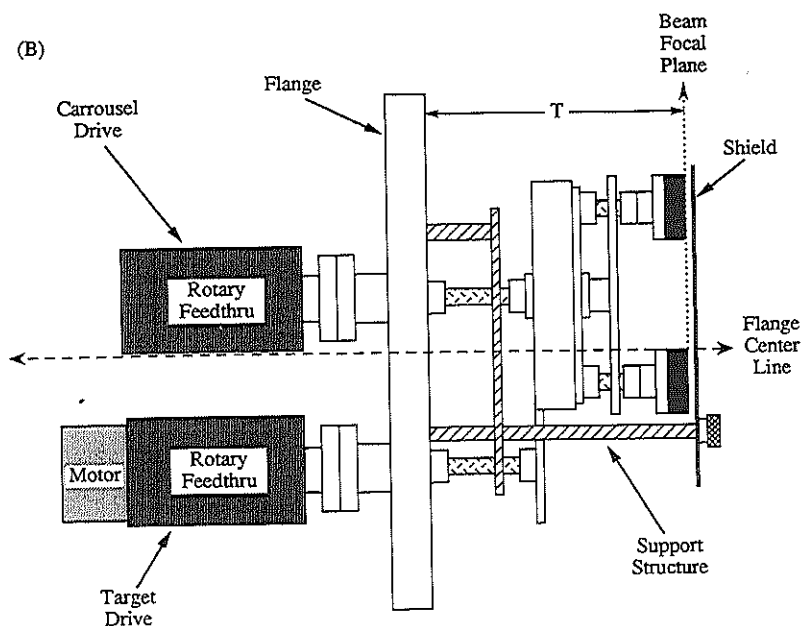
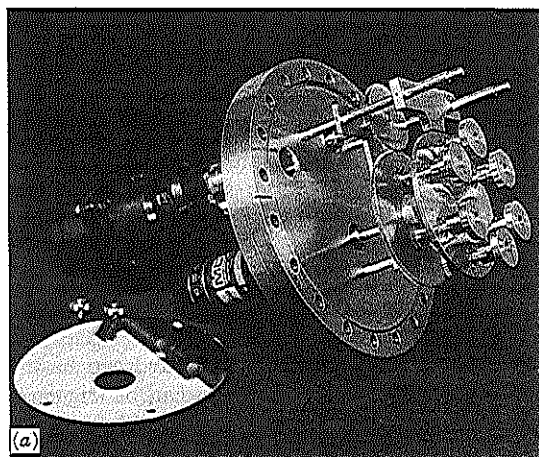


Figure 2.9. Target Carousel Flange Assembly for in situ multilayer depositions. (A) Photo courtesy of Neocera, Inc. (B) Schematic diagram indicating the various components and parameters important to the Carrousel design.



Figure 2.10. A commercially available automated multilayer deposition accessory for PLD. (Photo courtesy of Neocera, Inc.)

complex. Resistive heaters formed from molybdenum foils or Nichrome wire can be rigged in the laboratory, and radiative methods such as quartz lamps can also be used. In addition to the power feedthroughs for the heater, allowance should be made for measuring the substrate temperature with, for example, a thermocouple.

As the need for temperature uniformity increases, so does the complexity of the substrate heater. Temperature uniformity criteria become critical when the formation energy of the desired compound or the need for epitaxy forces the temperature into a narrow band. Bonding of the substrate to the substrate heater is perhaps the most common method of improving temperature uniformity. For example, cable heaters brazed to a nickel plate create nice flat-plate heaters to which substrates can be bonded.

In choosing the bonding medium, attention should be given to the maximum service temperature, outgassing, thermal conductivity, and ease of substrate removal. Many silver paints, such as those used commonly for scanning electron microscope sample preparation, work well. If deposition temperatures of a few hundred degrees must be maintained over surface areas on the order of  $1 \text{ cm}^2$  to within a few degrees, the mechanical bond is usually quite strong. In this case, one needs to consider how best to remove the substrate from the

flat-plate heater. A rugged substrate heater support assembly is therefore highly recommended.

There are several substrate heaters which are commercially available. Basically, these heaters differ in four areas which are: (a) the material used in the heater assembly construction, (b) the type of heating element used, (c) whether or not the heater is oxygen compatible, and (d) the maximum temperature to which it is rated. A commercially available flat plate substrate heater assembly is displayed in Figure 2.11.

#### 2.4.4 Pumps, Gas flow, and Vacuum gauges

One of the advantages of PLD as compared to other film deposition techniques is that it requires very simple and relatively economical pumping and gas-flow systems. As a matter of fact, metal oxide epitaxial films have been grown by using a simple six-way cross pumped by an oil-seal mechanical pump, with the  $O_2$  gas flow regulated by a single-needle metering valve and the pressure measured with a thermocouple gauge. Such a system, however, is likely to be subject to oil contamination from the pump and to poor reproducibility from sample to sample due to difficulties in controlling the deposition parameters (e.g., deposition pressure, gas flow, and poor system cleanliness due to the high base pressure).

When choosing the type of vacuum pump for a PLD system, it is worth considering the following points. As with most thin-film deposition techniques, maintaining a clean, dust-free, and oil-free environment is important. Depending on the nature of the gas being pumped (e.g., oxygen), corrosion-resistant pumps might be required in order to guarantee the safe operation and long life of the system. For depositing metal oxides and other complex structures, a high gas pressure might be required necessitating the use of high gas throughput and pumps capable of operating at high pressure. Space considerations and fast cycling from atmosphere to vacuum might be important when designing a system requiring a small footprint and high sample throughput. Finally, price and maintenance costs should also be considered.

In general, any high vacuum pumping system can be adapted for use on a PLD system. However, using corrosion-resistant molecular drag pumps (MDPs) or hybrid turbomolecular drag pumps with a diaphragm pump in their foreline can provide the best alternative. These pumps provide enough advantages when used in a PLD system as compared with other pumping arrangements, so that their initial high cost (ranging from \$6K to \$15K) should not be considered a serious objection.

A well-designed gas-flow system and the use of appropriate vacuum gauges will allow for careful control of the gas flow and pressures during and after the deposition. Again several alternatives are available with a characteristic scaling of price with sophistication. A combination of a needle metering valve and a column flowmeter is a very economical way of controlling and measuring the

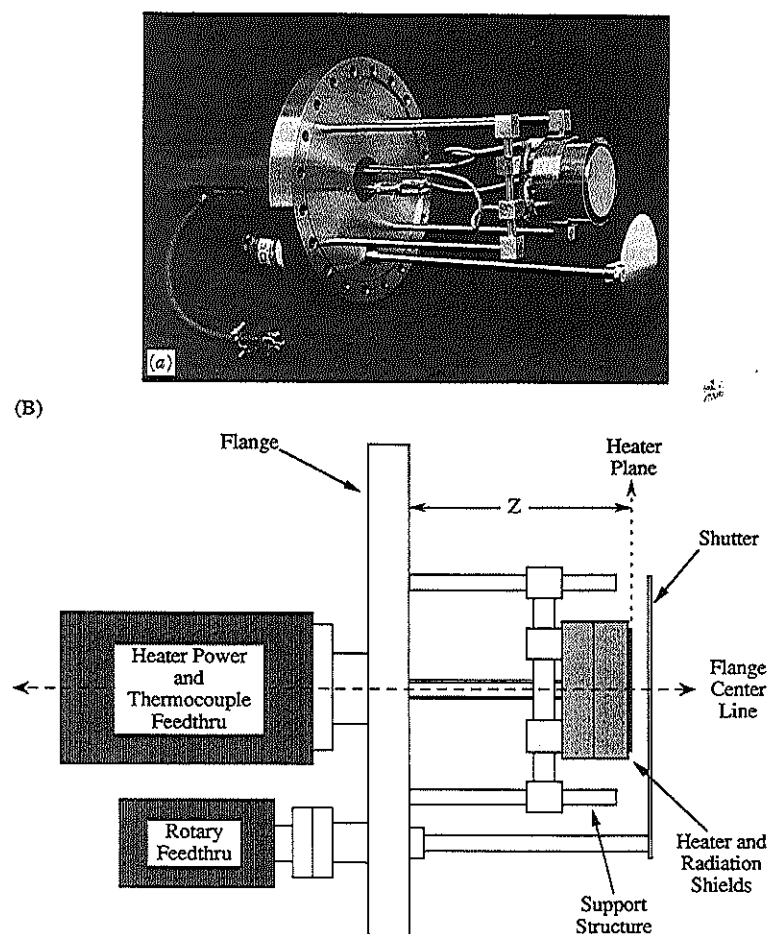


Figure 2.11. A commercially available substrate heater flange assembly. (A) Photo courtesy of Neocera, Inc. (B) Schematic diagram indicating the various components and parameters important to the heater design.

flow of gas during the deposition. More sophisticated mass flow controllers can be used when the need for high accuracy and computer control arises.

In choosing the appropriate vacuum gauge for the system, it is worth considering the fact that PLD of various materials may be performed with background pressures ranging from 500 mtorr to less than 1 mtorr, combined with an annealing step that requires pressures on the order of several hundred torr. By using convectron-type vacuum gauges, it is possible to measure



reliably each of these pressures with a single gauge and controller. If an ionization gauge needs to be used in order to measure pressures below 0.5 mtorr, however, it is recommended that a cold cathode type of ionization gauge be used. This will avoid premature gauge failure due to the filament burning out when the background gas is introduced into the system.

All the components mentioned in this section are readily available from several pumping and vacuum gauge manufacturers. New vacuum pumps and gauges are frequently introduced into the market so that even more alternatives will be available in the near future. Companies that offer complete PLD systems, such as Neocera, Kurt J. Lesker, and Fermi Systems and Instruments should be able to recommend the best choices for pumps and other vacuum accessories.

#### 2.4.5 Particle Filters

PLD allows for the use of a wide variety of targets. One drawback, however, is the fact that large particles tend to be generated from the target material and become embedded in the films. These particles, which range in size from  $<0.1$  to several microns in diameter, can destroy the integrity of multilayer films, produce film layers with very rough surfaces, and make the patterning of small features onto the film very difficult. The last point is very important if devices with small dimensions are to be fabricated from such films.

The subject of particulates and their origin is discussed thoroughly in a separate chapter of this book. Here, we mention one possible device that can mitigate the problem of particulates: a particle filter. Such a filter must be able to block the passage of particles and other agglomerates, but allow the atomic and molecular evaporants to pass through.

There are several ways of achieving this goal, and all take advantage of the differences in size and velocity between the material being evaporated and the particles being ejected. Among the different types of filters used, we mention here those that are based on electrostatic deflection and those that use mechanical trapping of the particles. By applying a bias voltage to the substrate heater, the charged particles can be repelled. In addition, if a biased cylindrical electrode surrounds the plume path, then the deflection of the particles will be even more efficient. The success of such filters, however, resides in the degree to which the large-sized particles are electrically charged that might vary depending on the material being ablated.

Mechanical trapping of the particles takes advantage of the fact that the particles ejected from the target move with slow velocities (less than 50 m/s) when compared with the atomic and molecular species (with velocities ranging from 100 to 5000 m/s). Such filters can be built by utilizing a rotating vane velocity filter, or a shutter synchronized with the laser pulse. The use of shutters is nontrivial when large-area depositions are required since a large shutter opening would be required to have a very short exposure time (about 1 ms).

A rotating vane filter, on the other hand, is very efficient in blocking

particles traveling at speeds less than a critical axial velocity,  $v_c$ , which is a function of the angular velocity, and the number and length of the vanes. Figure 2.12 shows a prototype of such a filter. By using high-speed vacuum-compatible motors (capable of reaching speeds above 30,000 rpm), a velocity filter can be built that will effectively reduce the number of particles deposited. Such filters place high demands on the vanes and bearings, which makes them susceptible to damage. At present, commercial particle filters are not yet available.

## 2.5 SAFETY

Excimer lasers are designated as class IV lasers. The appropriate measures for handling this class of laser should be taken into account when designing the laser facility. Because the excimer emits UV light, there are some simple precautions that should be followed to eliminate potential hazards. As with any high-output laser, the eyes need to be protected. Plastic safety glasses with side shields usually will do the job. One can also purchase laser safety goggles specifically for excimer lasers.

Direct exposure of the excimer output to the skin should also be minimized. As long as the bare skin remains out of the beam and there is minimal scattering of the light, the potential for danger is low. You have a better chance of being burned spending a few hours outside in the hot sun. Just the same, it is wise to block any radiation that will be scattered off of the external optics, such as the lenses, mirrors, and windows. Most plastic sheets, such as clear acrylic, will act to completely absorb any scattered UV. In many facilities, it will be a requirement to completely enclose the beam, from laser to deposition chamber. It may also be necessary to provide door interlocks and warning

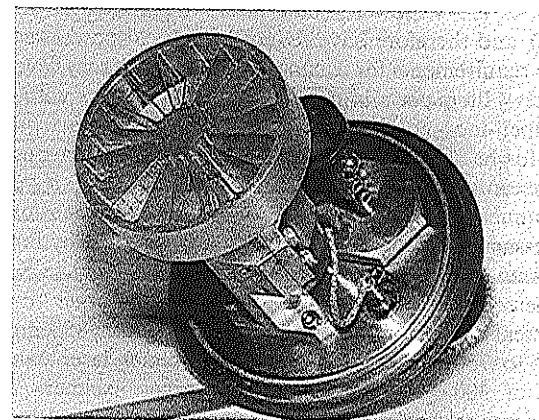


Figure 2.12. A prototype particle velocity filter. (Photo courtesy of Neocera, Inc.)

lights. Before operating your PLD system, the Safety Office for your facility should be consulted regarding any rules that may apply.

The potential health hazard and corrosive nature of the halogen gas component of the excimer laser requires a safe gas delivery system. Halogens, such as chlorine and fluorine, react with tissue and mucous membranes to produce acids. Fortunately, our olfactory system is an excellent halogen detector. So trust your nose and move to a well-ventilated area should any leaks be detected. All gas bottles should reside in an industry-approved gas cabinet that is properly vented. For safe operation, the ventilation system must be able to draw a minimum of 200 ft<sup>3</sup>/min. A safe system illustrating operation from separate gas bottles is shown in Figure 2.13. The initial capital investment for such a system can be in the neighborhood of \$5000 to \$7000. Consult with the Safety Office for your facility to determine the specific regulations that apply.

## 2.6 FACILITIES

There are several factors relevant to excimer lasers that need consideration when designing a PLD facility. The electrical, cooling, spatial, and safety requirements should be taken into account in order to ensure a smooth integration of the laser into the PLD facility. The following paragraphs provide a brief overview of these requirements.

Essentially all of the electric-discharge-pumped excimers that have been installed over the years operate from three-phase 208-V electrical power. The laser output power (pulse energy  $\times$  repetition rate) determines the electrical current requirements, which can range from 20-A service at the low end to as much as 80-A service for the largest UV cannons. Recently, a new line of excimer lasers has been introduced (Lambda Physik Lextra series) that operate from single-phase 115-V power. These lasers are limited to lower repetition rates (<30 Hz), and therefore have reduced electrical power requirements.

The cooling requirements for excimer lasers are not very severe. Water flow rates of less than 4 liters per minute are sufficient for lasers with output powers up to 80 W. Open-loop cooling systems using ordinary tap water (filters are recommended for hard water) as well as closed-loop systems using water and antifreeze are acceptable. In some instances, the use of an external water chiller might be recommended. For the low duty cycle lasers mentioned earlier, no coolant is necessary. These lasers are convectively cooled by forced air.

Based on some of the performance specifications given in Section 2.1, one might have guessed that excimer lasers are certainly larger than the average bread box. Typical dimensions can be 2000 mm in length, 850 mm in width, and about 450 mm to 750 mm tall. The average excimer laser can weigh in the neighborhood of 300 to 400 kg, with the larger excimers having weight specifications as much as 500 kg. An appropriate optical table or sturdy boxed-section frame will usually suffice for supporting the excimer.

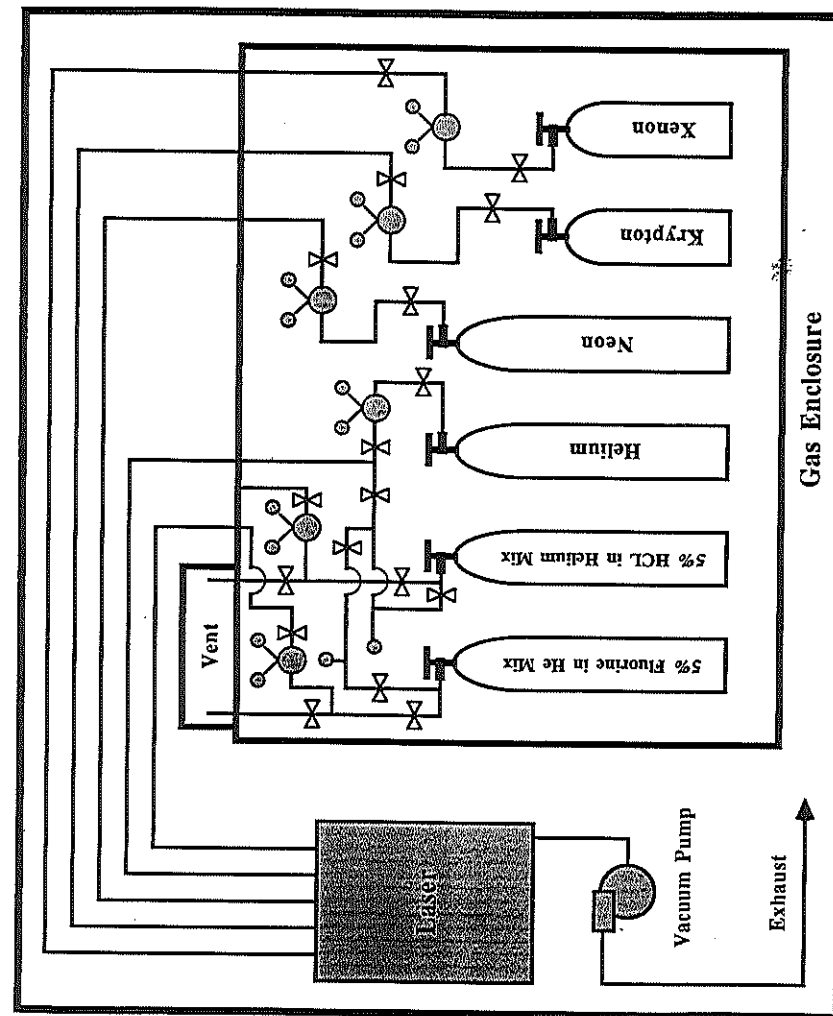


Figure 2.13. Diagram illustrating a safe gas handling system for excimer gases.



The manner in which the optics will be mounted should be given consideration, particularly if more than one deposition system will be coupled to the laser beam via mirrors and beam splitters. Fine adjustment of lenses, mirrors, and beam splitters could be required. Thus, these elements should be located within easy reach of the deposition system operator. Any enclosures that are required for safety purposes must permit ready access to the optics contained within. While optical tables are probably not necessary (since small vibrations will likely not disrupt the deposition process), optical breadboards and slide mounts are recommended to facilitate fine adjustment. Also, magnetic mounts are recommended for the mirrors and beam splitters that might have to be removed and replaced in a reproducible fashion (see Figure 2.6).

Another issue to consider is the peripheral test and measurement apparatus required by the laser. The laser operator will generally want to measure the laser output energy and/or look at the pulse-to-pulse stability on a daily basis. A pyroelectric energy detector is best suited for this purpose. Because of the large beam size of excimer lasers, a large aperture detector is best suited. If the laser is to be operated at high repetition rates ( $> 20$  Hz), it may be of interest to know the output power. A calorimeter-type power probe, or "meat stick," is used for this purpose. Typically these probes have readout scales calibrated for a 20-s exposure. Dividing the scale reading by the repetition rate allows one to back out the average laser pulse energy. For diagnostic purposes one may want to look at the temporal shape of the laser pulse. The pulse duration of a typical excimer has a full width at half maximum (FWHM) of 20–30 ns. A vacuum photodiode (risetime  $< 0.5$  ns) and fast oscilloscope ( $\sim 350$  MHz) are needed to fully resolve the pulse shape.

As indicated earlier, the beam profile is an important laser parameter for PLD work. There are a variety of ways to examine the beam profile. Ordinary burn paper or thermal fax paper is useful to a certain degree. It can be used to help align the cavity optics and check the beam profile at various points in the optical setup. On the other hand, the paper saturates easily and therefore does not give a complete picture of the beam profile. A beam profiling system incorporating a CCD camera is required for complete diagnostics and real-time monitoring of the spatial output characteristics. The camera systems provide the most information in the least amount of time and allow for digital documentation capabilities. These systems can be expensive, however, so one must determine whether the application warrants the expense. An alternative and much less expensive method of analyzing beam characteristics is the use of UV-absorbing films. These films change color when exposed to ultraviolet light. Below a certain threshold the color change is linearly proportional to the energy density in the beam, and thus a fairly accurate picture of the energy distribution can be obtained. Using a microdensitometer, one can digitally document the beam profile.

A final thing to consider when purchasing an excimer is the compatibility of the laser with other equipment in the PLD facility. Because of the high-voltage discharge, one might expect the excimer laser to be a good source

of electromagnetic interference (EMI) noise. In fact, this is quite true. However, EMI does not pose a problem if the excimer engineers have properly designed the shielding. Internally, EMI problems have been eliminated from excimer lasers by the use of local-area fiber optic networks. All logic signals for triggering, gas handling, energy monitor readings, and so forth, are piped around the laser via optical fibers. Hence, no false signals are induced by EMI noise.

This chapter has provided a foundation for the development of a PLD facility. Three primary topics were covered: lasers, optics, and deposition systems. In addition, basic safety and facility requirements were covered as separate topics. It is hoped that this chapter will not only serve as a useful introduction for those researchers who wish to begin PLD research from scratch, but also serve as a useful reference guide to those who currently use PLD in their laboratories.

## 2.7 SUPPLIERS

As with most equipment, familiarity with "off-the-shelf" components and available systems is highly recommended. Table 2.4 is a partial list of suppliers

**TABLE 2.4 Suppliers of Pulsed Laser Deposition Equipment and Associated Components**

Product and Company	Location	Phone Number
Excimer Lasers		
Lambda Physik, Inc.	Acton, MA.	508-263-1100
Lumonics Inc.	Livonia, MI.	313-591-0101
Deposition Systems and Components		
Neocera, Inc.	College Park, MD.	301-314-9937
Riber, Inc.	Edison, NJ.	908-494-8860
Conductus, Inc.	Sunnyvale, CA.	408-737-6700
Kurt J. Lesker Company	Clairton, PA.	412-233-4200
Thermionics Northwest, Inc.	Port Townsend, WA.	206-385-7707
Fermi Systems and Instruments, Inc.	Buffalo, NY.	716-833-7534
Gas Suppliers		
Air Products	Allentown, PA.	215-481-8257
Spectra Gases	Irvington, NJ.	201-372-2060
Laser Detectors		
Coherent, Inc.	Auburn, CA.	916-885-6039
Gentec Inc.	Palo Alto, CA.	415-321-4258
Optical Engineering	Santa Rosa, CA.	707-528-1080
Sciencetech, Inc.	Boulder, CO.	303-444-1361
UV optics		
Acton Research Corporation	Acton, MA.	508-263-3584
Rocky Mountain Instrument Company	Longmont, CO.	303-651-2211

that is by no means exhaustive. Before settling on a design for your system, it is highly recommended that you establish contact with these or other companies in order to achieve interchangeability, and to avoid the added costs associated with customized components.

## REFERENCES

- Basting, D., K. Mohla, E. Albers, and M. V. Bergmann. (1984). *Lasers and Optoelektronik* 2, 128-131.
- Yariv, A. (1976). *Introduction to Optical Electronics*, 2d ed., Holt, Rinehart & Winston, New York.

## CHAPTER 3

# MECHANISMS OF PULSED LASER SPUTTERING

ROGER KELLY

Dipartimento di Fisica  
Università di Trento and  
Istituto per la Ricerca Scientifica e Tecnologica  
I-38050 Povo (Trento), Italy

ANTONIO MIOTELLO

Dipartimento di Fisica and  
Consorzio Interuniversitario Nazionale Fisica della Materia  
Università di Trento  
I-38050 Povo (Trento), Italy

## 3.1 INTRODUCTION

The work of the past two decades has clarified most of the *primary* sputtering mechanisms relevant when condensed phases are bombarded with ions, electrons, single photons, or pulsed photons, that is, laser pulses. This sputtering leads to particle emission, also commonly termed *ablation* or *desorption*. Mechanistic possibilities include the ensemble of processes established in work with ions and electrons, namely *collisional*, *thermal*, *electronic*, and *exfoliation*, together with the formation of *clusters* by condensation. The only substantially new process arising with pulsed photons is the emission of droplets, that is, *hydrodynamic* sputtering. Table 3.1 indicates which mechanisms have been attested for different incident species. These primary sputtering mechanisms are in general well understood.

We are here concerned exclusively with pulsed photon sputtering and would note that the term *pulsed photons* normally refers to a laser pulse, often that of an excimer laser, but may in the near future refer to pulses of synchrotron radiation. Also, one can anticipate a future situation in which pulsed electrons (Donà dalle Rose et al., 1983) or ions (Brown et al., 1991) play a role in sputtering and not just in annealing. Bombardments with pulses of particles

TABLE 3.1 Occurrence of Primary Sputtering Mechanisms for Different Incident Species

Mechanism	Incident Ions	Incident Electrons	Incident Single Photons	Incident Pulsed Photons
Collisional	Yes	Yes	No	No <sup>a</sup>
Thermal (vaporization)	?	No	No	Yes
( $T > T_c$ )	Yes	?	No	Yes
Electronic				
(not plasmon-induced)	Yes	Yes	Yes	Yes
(plasmon-induced)	?	?	?	Yes
Macroscopic				
(exfoliation)	Yes	No	No	Yes
(hydrodynamic)	No	No	No	Yes
(condensational)	Yes	?	?	Yes

Source: Kelly et al., 1992a.

<sup>a</sup>But indirect collisional effects are possible due to ions formed by laser-plasma interaction.

differ fundamentally from bombardments with single particles in that the emitted particles often have a sufficiently high density that they interact, lose memory of the *primary* mechanism, and are therefore better described in terms of what we will call a *secondary* mechanism. This occasionally happens also with incident ions, but only when the yield is unusually high (Urbassek and Michl, 1987; Kelly, 1990a; Wien, 1992). At least four secondary mechanisms are currently understood: *outflow* either with reflection or recondensation, as when a finite reservoir expands, and *effusion* with either reflection or recondensation as for effusive release from the outer surface of a target (Table 3.2). "Reflection" and "recondensation" here refer to the behavior of particles backscattered towards the surface.

The following abbreviations will be used in what follows: KL = Knudsen layer, LOC = line of contact (where the density profile shows an abrupt change of slope),  $M = u/a$  = Mach number, SEM = scanning electron microscopy,  $T_c$  = thermodynamic critical temperature (where the vapor and liquid have the same density), TOF = time of flight, UAE = unsteady adiabatic expansion (i.e., an adiabatic expansion that is time dependent). Concerning terminology, we use "energy density" and "fluence" interchangeably, and prefer "sputtering" to the various synonyms such as "ablation" or "desorption."

From a mathematical point of view, the existence of the secondary mechanisms means that the emitted particles tend to move according to the laws of gas-dynamics. For planar (i.e., one-dimensional) motion the following pair of coupled flow equations will apply (Reif, 1965; Kelly, 1990b and 1992; Sibold

TABLE 3.2 Classification of Terminating Expansions

Basic Process	Knudsen Layer?	Behavior of Particles Backscattered Toward the Surface	Condensation Efficiency	Suggested Name <sup>a</sup>
Wall removal	No	Reflection	0	Outflow with reflection ( <i>outflow</i> )
	No	Recondensation	1	Outflow with recondensation
Effusionlike	Yes	Reflection	0	Effusion with reflection ( <i>effusion</i> )
	Yes	Recondensation	1	Effusion with recondensation ( <i>recondensation</i> )

Source: From Kelly and Miotello, 1993.

<sup>a</sup>There is apparently no established terminology to describe the various types of expansion, with a different choice being made, for example, by Kelly and Braren (1991) (shown in brackets).

and Urbassek, 1992):

$$\begin{aligned} \frac{\partial a}{\partial t} + u \frac{\partial a}{\partial x} + \frac{(\gamma - 1)a}{2} \frac{\partial u}{\partial x} &= 0 \quad (\text{continuity equation}) \\ \frac{\partial u}{\partial t} + u \frac{\partial u}{\partial x} + \frac{2a}{\gamma - 1} \frac{\partial a}{\partial x} &= 0 \quad (\text{Euler equation}) \end{aligned} \quad (3.1)$$

Here  $a = (\gamma k_B T/m)^{1/2}$  is the sound speed,  $u$  is the flow velocity,  $\gamma$  is the heat-capacity ratio, given by

$$\gamma = \frac{C_p}{C_v} = \frac{j + 5}{j + 3} \quad (3.2a)$$

and  $j$  is the number of internal degrees of freedom of the escaping particles accessible at the particular temperature. Note that for an adiabatic, reversible, isentropic expansion of a gas the mass density ( $\rho$ ), temperature, and sound speed are related by

$$\rho \propto T^{1/(\gamma-1)} \propto a^{2/(\gamma-1)} \quad (3.2b)$$

this being the reason why  $\rho$ ,  $T$ , and  $a$  do not all appear in Eqs. 3.1. Also, we note that the equation of state for a perfect gas is

$$p = nk_B T = \frac{\rho k_B T}{m} = \frac{\rho a^2}{\gamma} \quad (3.2c)$$

where  $p$  is the pressure,  $n = \rho/m$  is the number density, and  $m$  is the particle mass.

A somewhat different aspect of there being a high density of emitted particles is that interactions may occur between the laser pulse and the emitted particles. The simplest form taken by these interactions is such that a third flow equation, that for energy, plays a role (Knight, 1982; Vertes et al., 1989a):

$$\rho \frac{\partial e}{\partial t} + \rho u \frac{\partial e}{\partial x} + p \frac{\partial u}{\partial x} = \frac{\partial \Phi}{\partial x} \quad (3.3)$$

where  $e$  is the internal energy per unit mass and  $\Phi$  is the laser heat input into the escaping particles in units of J/cm<sup>2</sup>s. For  $\partial \Phi / \partial x = 0$  and the substitutions  $e = a^2 / \gamma (\gamma - 1)$  and  $p = \rho a^2 / \gamma$ , Eq. 3.3 becomes identical with the continuity equation, Eqs. 3.1. A still more complicated situation occurs when it is necessary to accommodate the interactions that occur when there is ionization (Vertes et al., 1989a, b).

The importance of gas-dynamic effects in pulsed laser bombardments was historically first accepted when it was realized that the emitted particles often showed either *forward peaking* (Namiki et al., 1986) or an unexpected *TOF temperature* (Dreyfus et al., 1987). In favorable cases both were confirmed (Wien, 1992). Concerning forward peaking, we expect, for small emitted particle densities, an angular distribution of the flux similar to the usual  $\cos \theta$ . With a KL, however, we expect roughly  $\cos^4 \theta$ , while with a UAE we expect  $\cos^8 \theta$  to  $\cos^{30} \theta$  (Section 3.3.1). Here  $\theta$  is the ejection polar angle. An example relevant to oxide sputtering is given in Figure 3.1, while for examples relevant to polymer and semiconductor sputtering we refer to Srinivasan et al. (1987) and Namiki et al. (1986). The point is that forward peaking in emitted particles, except in the unusual instances where it is inherent to the mechanism (Garrison and Srinivasan, 1985), is normally indicative of the operation of Eqs. 3.1–3.3, increasing with  $M = u/a$  (Kelly, 1990b; Saenger, 1991). Concerning unexpected TOF temperatures, the values for  $\theta = 0$  can be 2.5 or more times higher than expected and will also depend strongly on the angle of observation (Figure 3.2).

## 3.2 DESCRIPTION OF THE PRIMARY MECHANISMS

We here consider the different *primary* sputtering mechanisms appropriate to incident laser pulses and, in particular, how they might be manifested in two of the most powerful analytical tools. These are SEM and energy (i.e., temperature) measurement, with the latter normally accomplished with TOF.

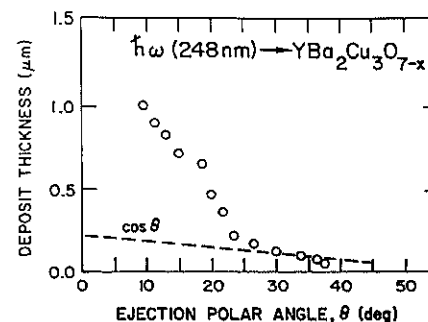


Figure 3.1. Example of strong forward peaking in the yield vs. polar angle,  $\theta$ , for the pulsed laser sputtering of  $\text{YBa}_2\text{Cu}_3\text{O}_{7-x}$ . The pulse length was  $\sim 20$  ns. The data have the approximate form  $\cos^{11} \theta$ , as for  $M = u/a \approx 2.5$  (Kelly, 1990b), and from this we infer that there were both a KL and UAE. (From Venkatesan et al. 1988.)

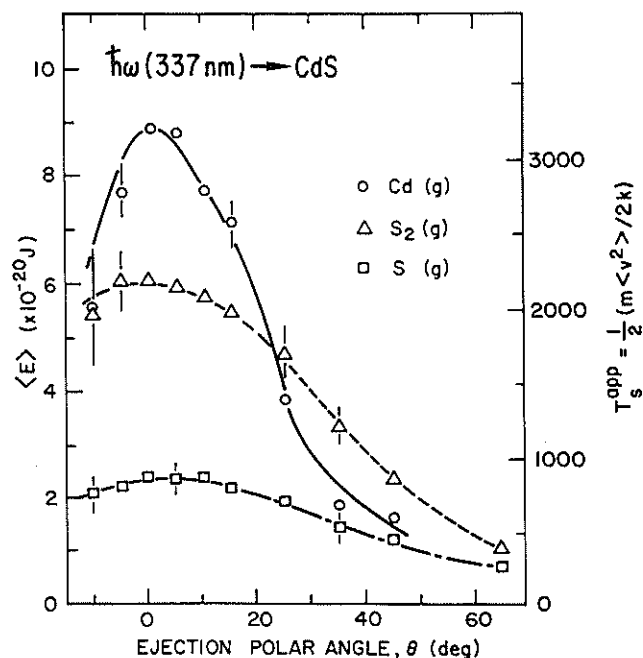


Figure 3.2. Examples of apparent TOF temperatures,  $T_s^{\text{app}}$ , vs. polar angle,  $\theta$ , for the pulsed laser sputtering of CdS. Temperatures measured normally to the target are distinctly too high, those measured obliquely are distinctly too low, and the normal temperatures increase with the mass of the emitted species. These effects are all characteristic of UAE, although the extent is rather greater than gas dynamics can explain. (From Namiki et al. 1986.)

The well established framework for ion sputtering (Kelly, 1984a, b) will be used where possible (Table 3.1).

### 3.2.1 Collisional Sputtering

Collisional sputtering in the sense of momentum transfer in direct beam-surface interactions cannot occur with laser pulses. To show this we consider the maximum ("") energy transfer,  $\hat{E}_2$ , in a binary collision between a particle with energy  $E_1$  and rest mass  $m_1$ , and a target atom with mass  $m_2$ . If relativistic effects are included and if  $M_i$  is the atomic weight, the expression is

$$\begin{aligned}\hat{E}_2 &= \frac{2E_1^2}{m_2c^2} + \frac{4M_1M_2E_1}{(M_1 + M_2)^2} \\ &= \frac{E_1^2}{M_2} \times 2.147 \times 10^{-9} + \frac{4M_1M_2E_1}{(M_1 + M_2)^2} \text{ eV}\end{aligned}\quad (3.4)$$

Values of  $\hat{E}_2$  for photons, electrons, and  $\text{He}^+$  colliding with Al atoms are compared in Table 3.3. We note that photons transfer negligible energy, that the electrons of a high-voltage electron microscope can displace a small number of atoms, and that  $\text{He}^+$ , depending on the energy, either does or does not cause displacements. In reaching these conclusions we assume a displacement energy threshold of  $E_d = 25 \text{ eV}$ .

Indirect collisional effects do, however, exist with photons. It has been shown that if a plasma forms for any reason during laser-surface interaction in vacuum or air, then an explicit laser-plasma interaction begins. Ions in the plasma are accelerated to as much as 100–1000 eV (Akhsakhalyan et al., 1982a) and nearby surfaces are ion-bombarded (Akhsakhalyan et al., 1982b; Gaponov et al., 1977).

One indication of collisional effects lies with *cone formation*. It is well

TABLE 3.3 Maximum Energy Transfer for Binary Collisions Between Photons, Electrons, and  $\text{He}^+$  with Al Atoms

Particle	Energy (eV)	Relativistic Part of Maximum Energy Transfer (eV)	Total Maximum Energy Transfer ( $\hat{E}_2$ in eV)
Photon	10	$8.0 \times 10^{-9}$	$8.0 \times 10^{-9}$
	500,000	20	20
Electron	10	$8.0 \times 10^{-9}$	$8.1 \times 10^{-4}$
	500,000	20	61
$\text{He}^+$	10	$8.0 \times 10^{-9}$	4.5
	500,000	20	225,000

Note: Calculated with Eq. (3.4).

established that an ion-bombarded surface, if it is nonuniform for any reason, will go through a cone-formation cycle due to the angular variation of the sputtering yield (Figure 3.3). Cones can also be anticipated to form during ion bombardment from impurities and from scattering. For example, material dislodged from a mask could locally protect a surface from erosion and lead to topography indistinguishable from that due to intrinsic nonuniformity. The role of scattering includes the tendency for irregularities to direct ions to their bases. Concerning laser-surface interaction, cone formation occurs with  $\text{Al}_2\text{O}_3$  bombarded in air at  $2.5 \text{ J/cm}^2$  (Figure 3.4). The presence of an air plasma adequately accounts for the difference from  $\text{Al}_2\text{O}_3$  bombarded in vacuum (Figure 3.5a) and one concludes (tentatively, of course) that ion bombardment has occurred.

Another indication of collisional effects lies with substrate erosion. Akhsakhalyan et al. (1982b) found evidence that particles emitted from a laser-bombarded Cd target caused significant erosion of a nearby surface ( $0.02$  to  $0.12 \text{ nm/pulse}$ ). They used somewhat higher energy densities ( $4$ – $10 \text{ J/dm}^2$ ) than were used in the work with  $\text{Al}_2\text{O}_3$ , and the target, Cd, would have undergone massive vaporization. Thus, the temperature reached with a metal for  $4$ – $10 \text{ J/cm}^2$  exceeds  $3700 \text{ K}$  (Kelly and Rothenberg, 1985b), so that the Cd would

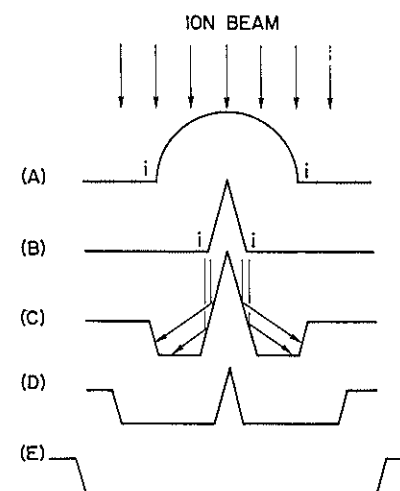
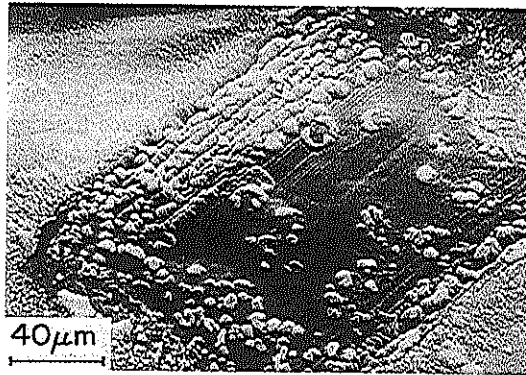
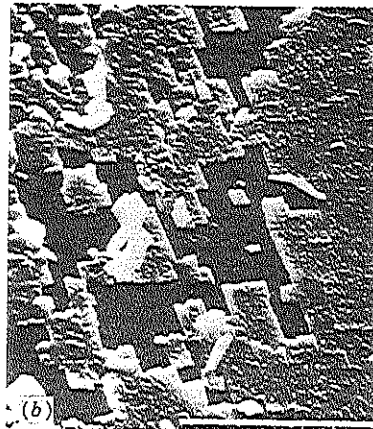
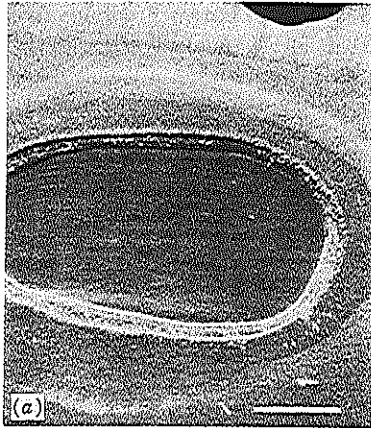


Figure 3.3. Sketches relevant to the evolution of an asperity on an ion-bombarded surface, the general ideas being valid also for pulsed laser bombardment when a plasma with energetic ions forms. (A) The asperity. (B) The cone into which (A) would evolve if the intersections, *i*, moved sufficiently far. (C) More correct situation showing the pit produced by scattering of the primary beam. (D) Shrinking of the cone relative to the pit. (E) Enlarged pit, which is the final configuration left after the cone disappears. (From Auciello and Kelly, 1982.)



**Figure 3.4.** Sputtering of single-crystalline  $\text{Al}_2\text{O}_3$  in air with 12-ns pulses of fluence  $2.5 \text{ J/cm}^2$  from a 193-nm ArF excimer laser. The number of pulses was 2880. A sputter crater is present containing cone-like topography that we assume to have been formed as in Figure 3.3. There is also a linear repetitive pattern with a spacing of  $1.2 \pm 0.2 \mu\text{m}$  and an irregular accumulation of material beyond the crater edges. (From Kelly et al. 1985.)



**Figure 3.5.** Sputtering of single-crystalline  $\text{Al}_2\text{O}_3$  in vacuum with 12-ns pulses of fluence  $\sim 0.5 \text{ J/cm}^2$  from a 248-nm KrF excimer laser. The number of pulses was  $\sim 1000$ . (a) Nuclei originally present have grown and coalesced until a single crater develops that is free of cones, exfoliates, and droplets. Further bombardment leads to a deepening of the crater and finally perforation of the specimen. Marker bar =  $500 \mu\text{m}$ . (b) Same as (a), but at higher magnification. This is a detailed view beyond the margin of the crater, showing that exfoliation occurs and that it tends to be crystallographic. Marker bar =  $50 \mu\text{m}$ . (From Rothenberg and Kelly, 1984.)

have vaporized at the rate appropriate to a vapor pressure exceeding 2000 atm. According to Eq. 3.5c below, 22 nm/pulse would have been removed. It is apparently this material, accelerated by laser-plasma interaction, that causes the erosion.

### 3.2.2 Thermal Sputtering

Thermal sputtering, in the sense of vaporization from a transiently heated target, may require temperatures well above the melting or boiling points. The reason is that the observed rate of laser sputtering (typically 1–10 nm/pulse) can be accomplished during the length of the release (“r”) process,  $\tau_r$ , only if the temperature is sufficiently high. The release time,  $\tau_r$ , is normally either shorter or longer than the laser pulse length,  $\tau$ . The temperature can never, on the other hand, exceed  $T_{rc}$  and claims to the contrary are simply wrong. This criticism remains true even if the energy distribution has a Maxwellian form (Section 3.3.1).

Let us consider the argument of Kelly et al. (1985) and Kelly and Rothenberg (1985) for describing thermal sputtering. Their argument is based on the usual expression for the vaporizing flux from a condensed phase:

$$\begin{aligned} \text{Vaporizing flux} &= \text{condensing flux} \\ &= p(2\pi m k_B T)^{-1/2} \\ &= p_0 \left\{ \exp \frac{-\Delta H_v}{k_B T} \right\} \times (2\pi m k_B T)^{-1/2} \text{ atoms/m}^2\text{s} \quad (3.5a) \end{aligned}$$

where  $p$  is the pressure that would exist if the equilibrium vapor were present,  $p_0$  is a constant defined by Eqs. 3.5a,  $\Delta H_v$  is the heat of vaporization (“v”), and the condensation efficiency (which enters into the condensing flux) has been taken as unity. The total loss from the target is then

$$\text{Depth/pulse} = \frac{p_0}{n_c} (2\pi m k_B)^{-1/2} \times \int_0^\infty \exp \left( \frac{-\Delta H_v}{k_B T} \right) T^{-1/2} dt \quad (3.5b)$$

where  $n_c$  is the number density of the condensed (“c”) phase. Equation 3.5b gives the asymptotic (“~”) result

$$\text{Depth/pulse} \sim (\hat{p}_{\text{atm}} \hat{T}^{1/2} \tau / M^{1/2} \Delta H_v) \times 1.53 \times 10^6 \text{ nm/pulse} \quad (3.5c)$$

where  $\hat{T}$  is the maximum surface temperature (ideally determined experimentally),  $M$  is the molecular weight of the vaporizing species,  $\Delta H_v$  is in electronvolts, and the pulse is assumed to have “top hat” form. Note the appearance of  $\tau$  and not  $\tau_r$  in Eq. 3.5c. Table 3.4 compares the temperatures for melting, boiling into 1 atm, and a vaporization rate of 1 nm/pulse. The latter are so



TABLE 3.4 Temperatures for Melting, Boiling, and a Vaporization Rate of 1 nm/pulse for Selected Solids

Solid	Melting Point (K)	Boiling Point at 1 atm (K)	Temperature for a Vaporization Rate of 1 nm/pulse (K)
Al	933	2793	3500
Au	1336	3133	4600
Cu	1356	2833	3800
Si	1685	3553	4600
W	3683	5828	>6000
Al <sub>2</sub> O <sub>3</sub>	2323	3850	4600
MgO	3098	3530	4200
SiO <sub>2</sub>	1995	3200	3800

Note: The temperatures for boiling and 1 nm/pulse were calculated, in the case of the oxides, from thermodynamic information, taking into account all possible vapor species (Chase et al., 1986). The temperature for 1 nm/pulse was evaluated from Eq. 3.5c with  $\tau = 12$  ns.

high that it is clear that, were they achieved, there would be strong evidence for melting accessible to SEM, for example wavelike structures as with Au (Figure 3.9, to follow). With Al, wavelike structures were reported to set in precisely at the melting point (Follstaedt et al., 1981).

It is worthwhile indicating that the following expression, occasionally used to describe vaporization from a transiently heated target (e.g., Batanov and Fedorov, 1973) is *not correct*:

$$\text{Depth/pulse} = \frac{I\tau}{n_s \Delta H_v} \quad (3.6)$$

where  $I$  is the laser heat input into the target in J/cm<sup>2</sup>s. For  $I\tau = 2.5$  J/cm<sup>2</sup>, Eq. 3.6 yields about 1  $\mu$ m/pulse for Al, and thus far too much compared with a typical sputtering rate of 1–10 nm/pulse. The problem is that Eq. 3.6 assumes the loss of material to be rate limited by conservation of energy, whereas the more correct Eqs. 3.5 assume the loss to be rate limited by kinetics. In particular, Eq. 3.6 does not take into account the surface temperature.

To clarify the role of the surface temperature, let us consider a *negative example*, that of Al<sub>2</sub>O<sub>3</sub>. As seen in Table 3.4 the condition for thermal sputtering of Al<sub>2</sub>O<sub>3</sub> at a rate of monolayers in nanoseconds is, very simply,  $T > 4600$  K. If 4600 K were reached, however, the specimens would have shown frozen wavelike surface topography indicative of melting and, possibly, evidence for droplet emission (Section 3.2.5). Such topography was normally *not* observed (Figures 3.4 and 3.5a), but the argument is not fully conclusive, as it is made without explicit knowledge of the surface temperature. Tempera-

tures were, however, obtained by TOF: provided the rotational and vibrational energies of ejected AlO can be taken as indicative of the real surface temperature, we conclude that the latter was  $< 1900$  K (Table 3.5). Particle emission is simply not possible at such low temperatures.

We finally note that there is a tendency in both contemporary and past work on pulsed laser sputtering to assume vaporization without adequate quantification. It is essential to remember in this connection that vaporization, unlike melting, is a slow process and must be described kinetically, as in Eqs. 3.5. Failing this, impossible postulates, such as the claim that 200 nm of SiO<sub>2</sub> can vaporize in 20 ps at 2400–2800 K, are made (Liu et al., 1981 and 1984).

### 3.2.3 Electronic Sputtering

Electronic sputtering is not a unique process, but rather a group of processes having the common feature of involving some form of excitation or ionization. It arises, for example, due to events as varied as ion explosions (Fleischer et al., 1965), the "hole-pair" mechanism (Itoh and Nakayama, 1982), defect formation (Nakai et al., 1991; Haglund and Kelly, 1993), or surface plasmon excitation (Helvajian and Welle, 1989; Hoheisel et al., 1991). It will normally fail to reveal itself in an explicit way in SEM, but will, by contrast, often be pinpointed convincingly by temperature information, especially the inequality,  $T \gg T_{ie}$ . It is normally confined to dielectrics and wide bandgap semiconductors, except when due to surface plasmons.

*High laser-pulse energies.* Let us now consider the specific example of Al<sub>2</sub>O<sub>3</sub> (Dreyfus et al., 1986). For high enough laser-pulse energies, dense electron excitation can be expected, perhaps as high as  $n_e \approx 10^{22}$  cm<sup>-3</sup>, where  $n_e$  is the excited electron-number density. As discussed by Wautelet and Laude (1980),

TABLE 3.5 Energies ( $i_B T$ ) and Temperatures of Al atoms and AlO Diatomics in the Etch Plume Formed by the Impact of KrF Excimer Laser Pulses on Al<sub>2</sub>O<sub>3</sub> or Oxidized Al in Vacuum

Type of Energy	Energies for Al <sub>2</sub> O <sub>3</sub> Target (eV)	Corresponding Temperatures (K)	Energies for Oxidized Al Target (eV)	Corresponding Temperatures (K)
Al, translational (i.e., kinetic)	3.5 <sup>a</sup>	(41,000) <sup>b</sup>	—	—
AlO, translational (i.e., kinetic)	1.1 <sup>a</sup>	(13,000) <sup>b</sup>	—	—
AlO, rotational	0.06–0.16	700–1900	0.06	700
AlO, vibrational	0.04–0.07	500–800	0.06	700

Source: Dreyfus et al., 1986.

<sup>a</sup>For a fluence near threshold,  $0.6 \pm 0.2$  J/cm<sup>2</sup>.

<sup>b</sup>Because of the inequality  $T \gg T_{ie}$ , these are clearly *not* real temperatures.

these electrons will increase the total energy of each atom by an amount similar to  $n_e E_{\text{gap}}/n_s$ , where  $E_{\text{gap}}$  is the energy gap. For a system like  $\text{Al}_2\text{O}_3$ , where  $E_{\text{gap}}$  is  $\sim 9 \text{ eV}$ ,  $n_s$  is  $4.7 \times 10^{22} (\text{Al atoms})/\text{cm}^3$ , and the depth of the potential well is  $5.7 \pm 0.1 \text{ eV}$ , it is clear that a value of  $n_e$  such as  $10^{22} \text{ cm}^{-3}$  would raise the energy of each atom by about  $2 \text{ eV}$ , and thus increase the vapor pressure by orders of magnitude or even render the lattice unbound.

We regard this model as related to the *rapid energy deposition* model (Jöst et al., 1982; Kissel and Krueger, 1987), which was devised to explain the unusual response of solids to incident particles ranging from laser pulses, to fission fragments, to electron pulses, to small accelerated dust particles. A possible description is that a rapid (i.e., nonadiabatic) transition takes individual ions directly into antibonding states. The result is that the system makes a transition from a tightly bound solid to a densely packed, repulsive gas, and particles are expelled energetically.

**Low laser-pulse energies.** Rapid energy deposition is not the only point of view, however, especially for low laser-pulse energies. As emphasized in work by Nakai et al. (1991) and Haglund and Kelly (1993), defects can form in and near the target surface, including self-trapped excitons and the decay products thereof (Figure 3.6) as well as damage revealed by low-energy electron diffraction (LEED). These defects, if they are formed at the surface or migrate to the surface, lead to the energetic expulsion of individual atoms.

The details of just what constitutes an electronic process are thus not straightforward, but the final result is clear. Particles are emitted that are characterized by a number of unusual features:

- Existence of a threshold energy density for particle emission (Figure 3.7);
- Kinetic energies of order of a few eV (Table 3.5);
- Low internal energies owing to a lack of equilibration during the energetic transition referred to in (b) (Table 3.5);
- High degree of directionality due to the close-packed nature of the starting material, a comportment that is, however, easily confused with forward peaking due to gas-dynamics (Figure 3.1);
- A nonthermodynamic yield of molecules,  $\text{AlO}$  in the case of  $\text{Al}_2\text{O}_3$ ;
- A nonthermodynamic yield of ions.

Significantly, these points also characterize the particles emitted by laser bombardment of oxidized Zr, effectively  $\text{ZrO}_2$  (Leismann et al., 1984). The internal energies were in this case determined from the populations of fine-structure levels of ground-state atoms. With  $\text{YBa}_2\text{Cu}_3\text{O}_{7-x}$  information on kinetic ( $2.4\text{--}6.5 \text{ eV}$ ) and internal ( $\sim 1000 \text{ K}$ ) energies is available (Otis and Goodwin, 1993) and may be taken, in our opinion, as suggesting that an

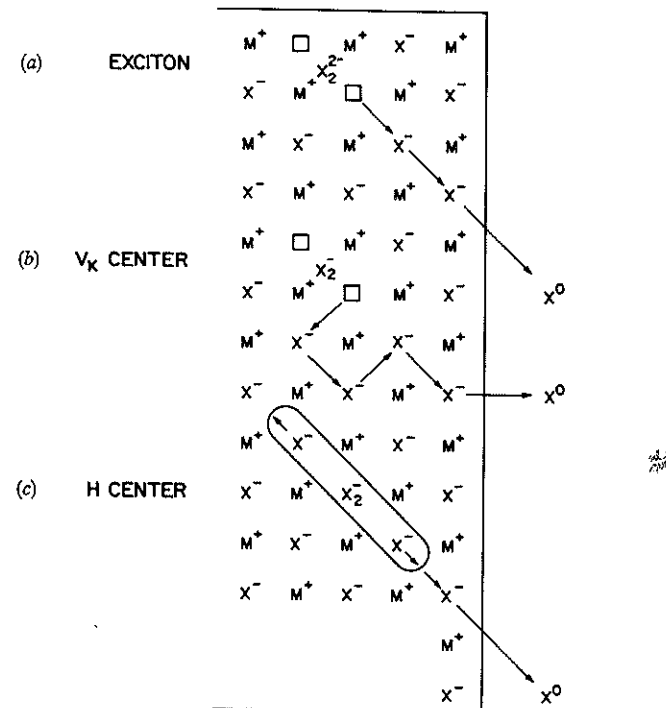


**Figure 3.6.** Generalized NaCl-type halide showing defects relevant to electronic sputtering. (a) A relaxed exciton with (110) symmetry. (b) A self-trapped hole or  $V_K$  center with (110) symmetry. (c) An  $H$  center, consisting of a crowdion-like neutral halogen interstitial. These defects are all able to diffuse at ambient temperature, while the exciton can, in addition, undergo nonradiative decay. The result in the case of the exciton and  $H$  center (but not the  $V_K$  center (Chen and Song, 1994)) is sputtering of halogen atoms from the surface.

electronic *primary* process was involved. That is, we take points (a)–(f) as constituting a sort of “fingerprint” for an electronic process.

### 3.2.4 Exfoliation Sputtering

Exfoliation sputtering, as when flakes detach from a target owing to repeated thermal shocks, would show an obvious and characteristic topography. It can be expected to occur whenever the system has a high linear thermal expansion ( $\Delta L/L_0$ ), where  $L_0$  is the thickness that is heated and  $\Delta L$  is the change in thickness, a high Young's modulus ( $E$ ), a high melting point ( $T_m$ ), and the laser-induced temperature excursions approach but do not exceed  $T_m$ . The



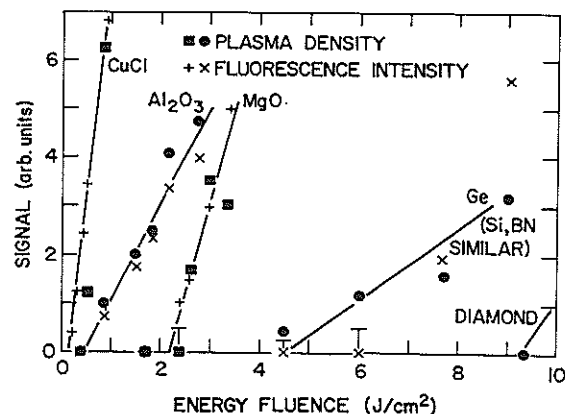


Figure 3.7. Comparison of the threshold fluences for particle emission for a number of solids that are bombarded in vacuum with 12-ns pulses from a 248-nm KrF excimer laser. In the case of plasma density, the threshold is for the measured free-electron density accompanying the particles; in the case of fluorescence, the threshold is for the intense optical emission. (From Dreyfus et al. 1986.)

thermal shocks would occur repeatedly and, since they were not relieved by melting, would finally lead to cracking.

We follow the argument of Kelly et al. (1985) for describing exfoliation sputtering. A convenient measure of thermal shock is the thermal stress,

$$\text{Stress} = \frac{E\Delta L}{L_0} \quad (3.7)$$

TABLE 3.6 Quantities Needed for Evaluating Thermal Stress by Means of Eq. 3.7

Solid	Linear Thermal Expansion of the Solid, <sup>a</sup> $\Delta L/L_0$	Young's Modulus, $E$ ( $10^{10} \times \text{Pa}$ )	$E\Delta L/L_0$ ( $10^{10} \times \text{Pa}$ )
Al	0.018	6.9	0.12
Au	0.018	8.0	0.14
Cu	0.021	11.1	0.23
Si	0.0054	11.3	0.06
W	0.023	34	0.78
$\text{Al}_2\text{O}_3$	0.020	47	0.94
MgO	0.045	26	1.2
$\text{SiO}_2$ (fused)	0.00077	7.2	0.006

Source: Kelly et al., 1985.

<sup>a</sup>Evaluated for the difference between 298 K and the melting point from explicit expressions for  $\Delta L/L_0$  (Touloukian et al., 1975).

The values of Eq. 3.7 as given in Table 3.6 suggest that exfoliation sputtering will occur with high melting metals such as W (therefore not Au, Figure 3.9, to follow) and with oxides such as  $\text{Al}_2\text{O}_3$  but not  $\text{SiO}_2$ .

Let us now consider the specific examples of W and  $\text{Al}_2\text{O}_3$ , both bombarded in vacuum. We failed to show macroscopic sputtering craters. Nevertheless, the prominent thermal-stress cracking led to random exfoliation as in Figure 3.8. In addition, it may be anticipated from the incipient droplets seen in Figure 3.8 that a hydrodynamic process becomes important at higher energy densities ( $>2.5 \text{ J/cm}^2$ ). With  $\text{Al}_2\text{O}_3$ , the relative smoothness of the craters (Figure 3.5a) suggests that collisional, exfoliation, and hydrodynamic processes are all unimportant, at least within the sputtered crater. Beyond the sputtered crater, however, the picture is completely different and prominent exfoliation is found (Figure 3.5b).

We finally note that exfoliation is also well known in heavy-ion bombardments (Braun et al., 1979). The mechanism is, however, unrelated to the thermal effects seen in Figures 3.5b and 3.8, being due instead to stresses caused by precipitation of the incident ions.

### 3.2.5 Hydrodynamic Sputtering

We use the term *hydrodynamic* to refer to processes in which droplets of material are formed and expelled from a target as a consequence of the transient melting, processes that have no analog in ion-surface interactions (Table 3.1). Evidence for such effects includes work on Au, as in Figure 3.9, and on other metals, as in Table 3.7. Droplets form also on polymer surfaces

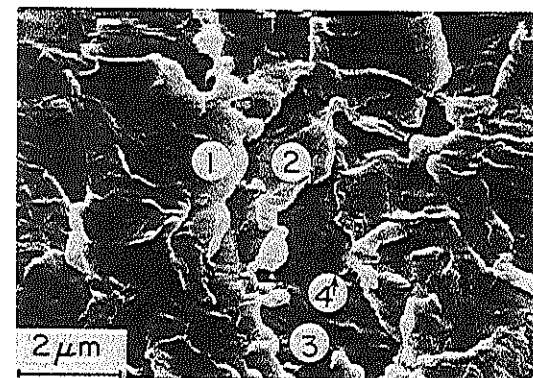
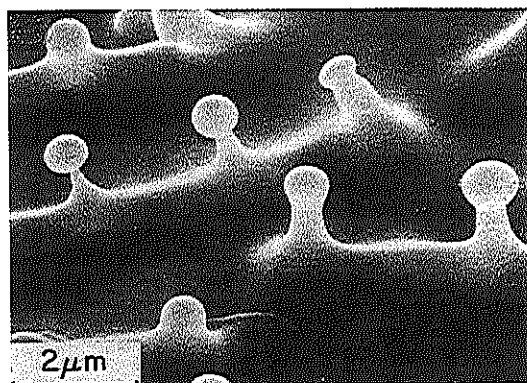


Figure 3.8. Sputtering of polycrystalline W in vacuum with 12-ns pulses of fluence  $2.5 \text{ J/cm}^2$  from a 193-nm ArF excimer laser. The number of pulses was 2000. Detailed view of the surface showing the topography to consist of exfoliation. The exfoliation is mostly incomplete, though a region labeled 1, 2, 3, 4 will be recognized where four generations of completed exfoliation can be identified. (From Kelly et al. 1985.)



**Figure 3.9.** Sputtering of polycrystalline Au in air with 12-ns pulses of fluence  $2.5 \text{ J/cm}^2$  from a 193-nm ArF excimer laser. The number of pulses was 4320. Detailed view of the surface showing wavelike ridges surmounted by droplets having diameters of  $0.9 \pm 0.2 \mu\text{m}$ . The droplets are in the process of being emitted from the ridges. (From Kelly et al. 1985.)

**TABLE 3.7** Quantities Needed for Evaluating the Minimum Droplet Size by Means of Eq. 3.9b

Metal	$\gamma$ , Surface Energy of Liquid ( $\text{J/m}^2$ )	$\alpha\Delta T$ , Linear Thermal Expansion of Liquid <sup>a</sup>	$(\rho_s - \rho_l/3\rho_s)$ , Linear Expansion Due to Melting	$\tilde{r}$ , Minimum Droplet Radius ( $\mu\text{m}$ )	Observed Droplet Radius ( $\mu\text{m}$ )
Al	0.866	0.086	0.021	1.0	2–5
Au	1.14	0.038	0.019	0.6	0.5
Pt	1.80	0.023	0.022	0.5	None
Bi	0.375	0.080	–0.010	~3	~4
PbTe	—	~0.027	~0.011	~3	~4
Cu	1.30	0.038	0.014	0.25	0.5
Si	0.730	0.038	–0.032	Probably none	None

*Note:* In general  $\tau$  was taken as 12 ns, except with Cu (1.7 ns), Bi (~100 ns), and PbTe (~100 ns). The value ~100 ns is an approximation to the rise time of the temperature (Knight, 1982) as distinct from the pulse length ( $6 \times 10^{-4}$  s). See Kelly and Rothenberg (1985). Droplets closely resembling those found with metals have also been observed with polymers (Novis et al., 1988; Nakata et al., 1993).

<sup>a</sup>The quantity  $\Delta T = \hat{T} - T_m$  was evaluated by taking  $\hat{T}$  as 2750 K.

(Novis et al., 1988; Nakata et al., 1993), though it is not known whether they are expelled as with metals.

To describe hydrodynamic sputtering we follow the thermal expansion argument of Kelly and Rothenberg (1985). We do not consider the alternatives based on the target recoiling due to the emitted particles (Batanov and Fedorov, 1973; Nakata et al., 1993) or based on differential etching (Novis et al., 1988). According to the thermal expansion model asperities somehow develop on the surface as in Figure 3.3a or 3.10a and, moreover, the laser-pulse energy is high enough for surface melting. The asperities are accelerated away from the melted substrate during each pulse, owing to the combination of the volume change on melting followed by thermal expansion of the liquid. That there might be motion of asperities away from the melted substrate requires that the melt depth ( $L_m$ ) be more or less uniform so that an asperity of height  $2r$ , as in Figure 3.10a, shows an additional total expansion  $\Delta L$ , as in Figure 3.10b. That the expansion during the heating is not counterbalanced by the behavior during the cooling follows because the cooling begins at the bottom of the melted substrate, so that, if anything, there is an additional tendency for the asperities to move away from the substrate. The turbulence of the surface, clearly visible in Figure 3.9, differential etching (Novis et al., 1988), as well as a variety of other effects, ensure that there are asperities that will participate in this expansion.

The alternative view (Batanov and Fedorov, 1973; Nakata et al., 1993), that recoil due to particle emission causes the fluid surface to flow, may contribute

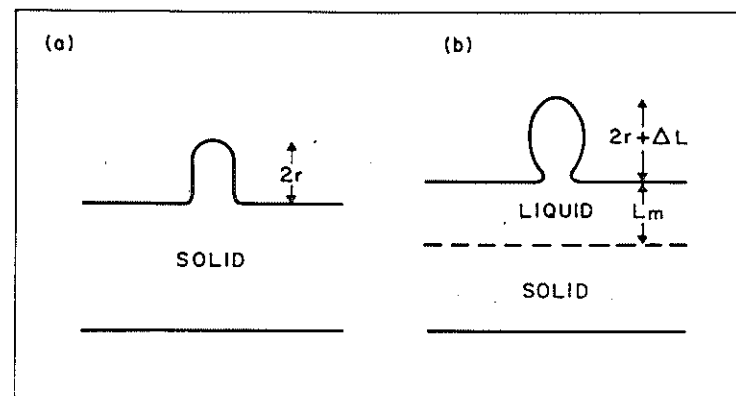


**Figure 3.10.** Sketch relevant to hydrodynamic sputtering. (a) A solidified asperity with a height of  $2r$  on a laser bombarded metal surface. The asperity could arise from a variety of effects, including turbulence and differential etching. (b) The same asperity while melted during a subsequent laser pulse. The melt depth of the liquid ( $L_m$ ) is assumed to be more or less uniform since the thermal time constant for a metal ( $L_m^2/\kappa \approx 1$ , ns) is much less than the laser pulse length,  $\tau$ . This in turn means that the asperity will show additional total expansion ( $\Delta L$ ) relative to the melted substrate.

to what is observed. There is a fundamental problem with such mechanisms, however, that in so far as the emission is due to vaporization it will be relatively slow below  $T_m$ : see Eqs. 3.5. Thermal expansion, by contrast, is effectively instantaneous.

The separation of asperities from the surface as droplets will be opposed, for a spherical shape, by a force

$$f = \frac{-\partial(4\pi r^2 \gamma)}{\partial r} = 8\pi r \gamma \quad (3.8)$$

where  $r$  is the droplet radius and  $\gamma$  is the liquid surface energy. A necessary condition for expulsion after a sufficient number of pulses is then that the total droplet momentum away from the substrate exceed the product  $f\Delta t$ , that is,

$$\frac{4\pi r^3 \rho_l \Delta L}{3 \Delta t} > 8\pi r \gamma \Delta t$$

$$\Delta L = 2\alpha \Delta T + 2r(\rho_s - \rho_l)/3\rho_s \quad (3.9a)$$

where  $\Delta L$  is the total height change of the droplet,  $\alpha$  is the linear thermal expansion coefficient of the liquid,  $\rho_s$  is the mass density of the solid,  $\rho_l$  is the mass density of the liquid,  $\Delta T$  is the difference  $\hat{T} - T_m$ ,  $\Delta t$  is the difference  $\tau - t_m$ , and  $t_m$  is the time at which  $T$  equals  $T_m$ , the melting point. Also,  $\hat{T}$  was determined experimentally to be  $2750 \pm 700$  K.

Equation 3.9a is readily rearranged to yield the minimum droplet size that can be expelled,  $\tilde{r}$ :

$$\tilde{r} = \left\{ \left( \frac{3\gamma L_0}{\rho_l \Delta L} \right) (\Delta t)^2 \right\}^{1/3} \quad (3.9b)$$

where we have introduced  $L_0 = 2r$ . Some of the quantities needed for evaluating Eq. 3.9b are given in Table 3.7.

It is seen from the final columns of Table 3.7 that the values deduced for  $\tilde{r}$  are in general comparable to the observed values.

### 3.3 DESCRIPTION OF THE SECONDARY MECHANISMS

#### 3.3.1 Definitions

For the abbreviations KL, LOC,  $M = u/a$ , SEM,  $T_m$ , TOF, and UAE, see Section 3.1, and for general references to this section, see Kelly and Braren (1991), Sibold and Urbassek (1992), Kelly et al. (1992a), and Kelly and Miotello (1993).

We here consider the different *secondary* sputtering mechanisms as are relevant with pulsed photon bombardments or, more generally, with other incident particles when the yield is very high (Urbassek and Michl, 1987; Kelly,

1990a; Wien, 1992). We suppose that photons strike a solid surface and that particles are therefore emitted in a pulse. When the density is small enough, the particles have  $v_x > 0$  and escape without interaction,  $v_x$  being the velocity normal to the target surface. In effect, they go into *free flight* and are described by whatever velocity distribution is appropriate to the *primary* sputtering mechanism. For example, a Maxwellian would be appropriate for thermal emission, but not otherwise.

When the quantity of particles per unit time is larger, of order 0.5 monolayer in nanoseconds (NoorBatcha et al., 1987 and 1988), the particles collide sufficiently that they come to equilibrium (Ytrehus, 1977; Cercignani, 1981; Kelly and Dreyfus, 1988a, b). They therefore have all  $v_x$ ,  $-\infty < v_x < +\infty$ , show a small flow velocity,

$$u_K = a_K = \left( \frac{\gamma k_B T_K}{m} \right)^{1/2}, \quad (3.10)$$

and show forward peaking with an angular distribution of the flux similar to  $\cos^4 \theta$ . This equilibration occurs in the so-called KL and, as is apparent from Eq. 3.10, has an outer boundary characterized by  $M = u_K/a_K = 1$ . (In Eq. 3.10 and elsewhere "K" refers to the KL boundary.) Rather independently of the primary velocity distribution, a Maxwellian form with  $v_x$  replaced by  $v_x - u_K$  can be expected whenever a KL forms. This is also termed a *shifted Maxwellian*:

$$f_K(v_x, v_y, v_z) = \frac{n_K}{(2\pi k_B T_K/m)^{3/2}} \frac{E_I^{(j/2-1)}}{\Gamma(j/2)(k_B T_K)^{j/2}}$$

$$\times \exp \left[ -\frac{2E_I + m\{(v_x - u_K)^2 + v_y^2 + v_z^2\}}{2k_B T_K} \right] \quad (3.11)$$

Here  $E_I$  is the total internal energy and  $j$  is the number of internal degrees of freedom of the escaping particles accessible at  $T_K$ . An important consequence of Eq. 3.11 is that, under conditions of collision, a Maxwellian form (with or without insignificant shifting) does not necessarily denote a thermal primary mechanism. This distinction is not always respected (Section 3.2.2). A schematic representation of KL formation followed by free flight is shown in Figure 3.11.

Without going into detail, we note that KL theory defines the ratios  $T_K/T_s$  and  $\rho_K/\rho_s$  for each  $\gamma$ , where  $s$  refers to the target surface. It also shows that a fraction  $F^-$  of the emitted particles is backscattered toward the surface and is conventionally assumed to recondense (Table 3.8). Under conditions of KL formation, a TOF spectrum with maximum velocity  $\hat{v}$  might be expected to yield a temperature

$$k_B T_s = \frac{m \hat{v}^2}{2} \frac{T_s}{T_K} \quad (3.12a)$$

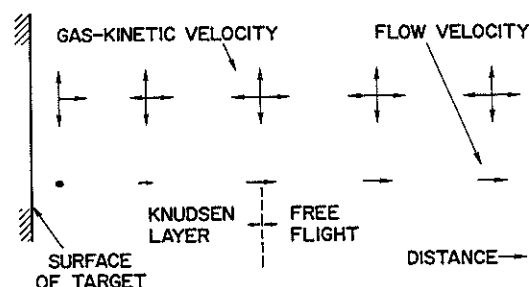


**Figure 3.11.** Schematic representation of a KL followed by free flight. A continuous, one-dimensional column of gas is assumed to be released from the target surface. The gas nearest the surface is characterized by  $v_x > 0$  and  $u = 0$ , while at the KL boundary the gas shows  $-\infty < v_x < +\infty$  and  $u = u_K$ . A surprisingly small number of collisions ( $\sim 3$ ; NoorBatcha et al., 1987 and 1988) is sufficient to establish the KL. The particles finally go into free flight and the velocities then persist unchanged.

but a more careful treatment in which the detailed form of the TOF spectrum is considered (Kelly and Dreyfus, 1988a, b) yields

$$k_B T_s = \frac{m \hat{v}^2}{2} \frac{T_s}{\eta T_K} \quad (3.12b)$$

with  $\eta T_K/T_s$  as in Table 3.9 (see  $M = u/a = 1$ ).

For still larger quantities of particles,  $\gg 1$  monolayer in nanoseconds, a UAE occurs governed by Eqs. 3.1–3.3. The result is that the flow velocity  $u_M$  increases beyond  $u_K$ , the sound speed  $a_M$  decreases below  $u_K$ , the ratio  $T_K/T_s$  evolves to  $T_M/T_s$ , and there is a more marked forward peaking in the flux as determined by  $M = u_M/a_M > 1$ . For example,  $\cos^{11} \theta$  is appropriate to the results shown in Figure 3.1, while forward peakings up to  $\cos^{50} \theta$  are known

**TABLE 3.8** Parameters to Describe a Fully Developed Knudsen Layer for  $M = u/a = 1$

Degrees of Internal Freedom, $j$	Heat-Capacity Ratio, $\gamma = C_p/C_v$ (Eq. 3.2a)	Temperature Ratio, $T_K/T_s$	Density Ratio, $\rho_K/\rho_s$	Backscattered Fraction, $F^-$
0	$\frac{5}{3}$	0.669	0.308	0.184
2	$\frac{7}{5}$	0.782	0.301	0.212
4	$\frac{9}{7}$	0.837	0.298	0.224
6	$\frac{11}{9}$	0.871	0.297	0.231
8	$\frac{13}{11}$	0.893	0.297	0.236
Infinity	1	1	0.296	0.257

Source: Kelly and Dreyfus, 1988a.

**TABLE 3.9** Values of  $T_M/T_s$  and of  $\eta T_M/T_s$  for Various Combinations of  $M = u/a$ ,  $\theta$ , and  $j$

$M = u/a$	$T_M/T_s$ ( $j = 0$ )	$\eta T_M/T_s$ for $\theta = 0^\circ$ ( $j = 0$ )	$\eta T_M/T_s$ for $\theta = 30^\circ$ ( $j = 0$ )	$\eta T_M/T_s$ for $\theta = 60^\circ$ ( $j = 0$ )	$\eta T_M/T_s$ for $\theta = 75^\circ$ ( $j = 0$ )
0	1	2	2	2	2
1	0.6691	2.53	2.32	1.85	1.58
2	0.4282	2.89	2.49	1.62	1.19
3	0.2974	3.31	2.73	1.51	0.977
4	0.2185	3.74	3.00	1.47	0.842
5	0.1673	4.13	3.25	1.46	0.754
	( $j = 4$ )	( $j = 4$ )	( $j = 4$ )	( $j = 4$ )	$\frac{1}{2} \eta T_M/T_s$ ( $j = 4$ )
0	1	2	2	2	2
1	0.8374	2.93	2.72	2.22	1.94
2	0.6617	3.90	3.41	2.32	1.77
3	0.5360	5.02	4.20	2.45	1.66
4	0.4429	6.20	5.03	2.61	1.58
5	0.3722	7.40	5.88	2.79	1.53

Note: The significance of  $\eta T_M/T_s$  is seen in Eqs. 3.12, that is,  $T_s$  is given by the temperature-like quantity  $m \hat{v}^2 / 2 k_B$  divided by  $\eta T_M/T_s$ . See Kelly (1990b).

from other work (Saenger 1993). Again a shifted Maxwellian velocity distribution can be expected, namely as in Eq. 3.11 but with  $u_K$  replaced by  $u_M$ . The same argument that led to Eq. 3.12b when only a KL is present now leads to

$$k_B T_s = \frac{m \hat{v}^2}{2} \frac{T_s}{\eta T_M} \quad (3.12c)$$

with  $\eta T_M/T_s$  as in Table 3.9 (see  $M = u/a > 1$ ). Information as in Table 3.9 would be used, for example, to derive  $T_s$  from Figure 3.2. It was used explicitly in studies of C (Dreyfus et al., 1987) and  $\text{Ca}(\text{OH})_2$  (Jodeh et al., 1993), and implicitly in a study of organic fragments (Wien, 1992).

Let us immediately note that the gas dynamics appropriate when a UAE occurs is *never* like the steady flow of gas in a tube of uniform diameter. Rather we have, as already noted in Section 3.1 and Table 3.2, the possibility, first of all, of *outflow*. This is a UAE as occurs when a gun is fired, which is equivalent to the wall in the sketch of Figure 3.12a being removed. Particles backscattered toward the target surface are variously *reflected* or *absorbed* (i.e., *recondensed*), leading to two types of outflow. A second possibility is *effusion*. This is a KL coupled to a UAE as occurs with ordinary vaporization, as when the wall in Figure 3.12b or c becomes porous. The process has two phases, the first (for

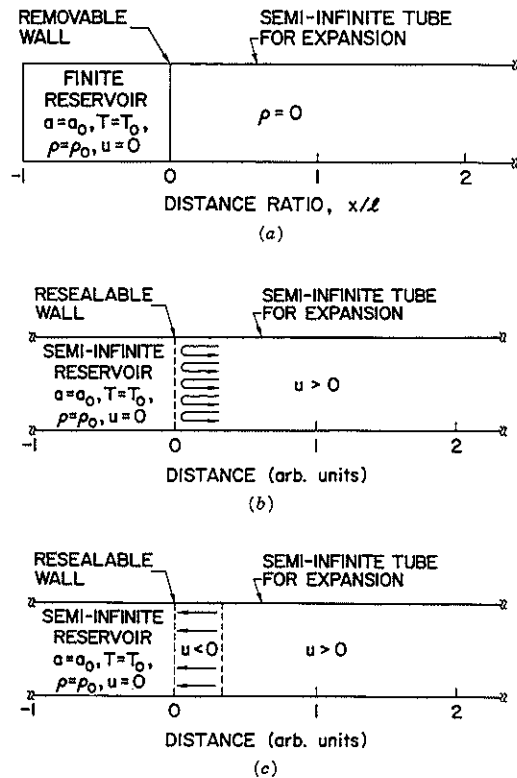


**Figure 3.12.** The different types of UAE. (a) *Outflow with either reflection or recondensation.* Gas in a finite reservoir escapes into vacuum when the wall is removed at  $t = 0$ . The resulting profiles of density vs. distance have analytical forms as in Figure 3.13 and can be photographed as in Figure 3.14. (b) *Effusion with reflection.* Gas in a semi-infinite reservoir effuses into vacuum from  $t = 0$  (when the wall becomes porous) to  $t = \tau_r$  (when the wall is resealed). Particles subsequently backscattered toward the wall are reflected, the resulting profiles of density vs. distance having analytical forms as in Figure 3.15. (c) *Effusion with recondensation.* Like (b) except that, for  $t > \tau_r$ , particles backscattered toward the wall are absorbed (i.e., recondensed). The resulting profiles of density vs. distance have analytical forms similar to those seen in Figure 3.15.

$0 \leq t \leq \tau_r$ ) constituting a UAE with a KL as described by Eq. 3.10 as the surface boundary condition. (The length of the *release process*,  $\tau_r$ , was introduced in Section 3.2.2.) The second phase begins when the release process ceases abruptly at  $t = \tau_r$ , as when the wall in Figure 3.12b or c is resealed. Again, particles backscattered toward the target surface are either *reflected* or *absorbed*, leading to two types of effusion.

In what follows we will normally assume that the target is bombarded in

vacuum and we will neglect the passage to free flight that occurs at low densities. In real systems there is often an ambient gas, so that the expansions terminate at a *contact front* when the densities are equal. Also, in real systems the role of gas dynamics ceases when the density is low enough that *free flight* sets in. The transition to free flight has been modeled with the “sudden freeze” approximation, in which collisions cease abruptly at a critical gas density (McClelland et al., 1979; Saenger, 1981 and 1991; Kelly, 1990b). Finally, we approximate the expansions as one-dimensional, as information on the more realistic three-dimensional expansions is very limited (Miotello et al., 1992; Urbassek and Sibold, 1993) and, as is clear from Figures 3.14 and 3.16, not altogether necessary.

### 3.3.2 Outflow with Reflection

As indicated earlier, outflow begins when, at  $t = 0$ , the system behaves as if a wall at  $x = 0$  is removed (Figure 3.12a). Physically this could come about if the arrival of a laser pulse caused a rapid passage to a gaslike condition, as when a condensed gas is brought to a temperature  $T > T_c$  (Urbassek and Michl, 1987; Kelly, 1990a) or a polymer suffers bond breakage (Braren et al., 1991; Garrison and Srinivasan, 1985). The only boundary condition when reflection occurs is given by  $u = 0$  at the back of the reservoir,  $x = -l$ . The problem resembles a gun, which is presumably why it was solved so early (Stanyukovich, 1960). The results for  $\gamma = \frac{5}{3}$ , expressed in terms of density versus distance, at first take the form shown by curves 0.5 and 1 in Figure 3.13. The

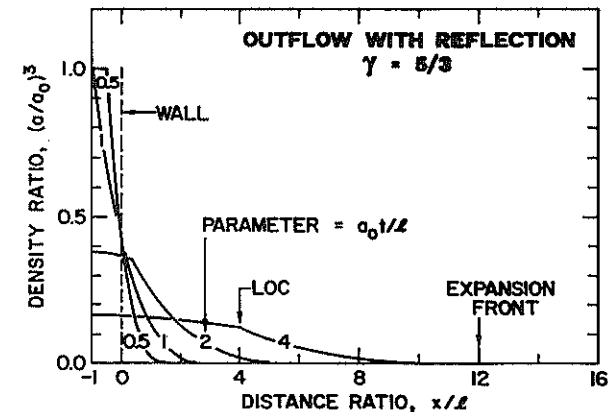


**Figure 3.13.** Calculated values of the density,  $\rho/\rho_0 = (a/a_0)^3$ , vs. the distance,  $x/l$ , for outflow with reflection. The problem is equivalent to that of a finite reservoir of gas as in Figure 3.12a. It is characterized initially by  $a_0$ ,  $T_0$ ,  $\rho_0$ , and  $u = 0$ , and is able to escape into vacuum when the wall is removed at  $t = 0$ . The indicated *expansion front* is that of the curve for  $a_0 t / l = 4$ .

density decreases from an unvarying value at the target surface ("wall") to zero at the *expansion front*. At the same time a rarefaction wave moves to the back of the reservoir, is reflected, and finally reaches the surface at time  $\tau_s$ :

$$\tau_s = \left( \frac{\gamma + 1}{2} \right)^{(\gamma+1)/2(\gamma-1)} \frac{l}{a_0} \approx \frac{\text{crater depth}}{\text{sound speed}} \quad (3.13)$$

where  $a_0$  is the sound speed in the undisturbed reservoir.

For  $t > \tau_s$ , the outflow continues without interruption and the results are typified by curves 2 and 4 in Figure 3.13. The density at the surface is seen to decrease though does not, it should be noted, fall to zero. The disturbance triggered by the rarefaction wave survives in the form of a LOC, which corresponds to an abrupt change of slope in the density profile. At the same time, the density profile has two parts, characterized, respectively, by near invariance and then a rapid decrease to the expansion front, the junction being the LOC. The particles at all times maintain contact with the target surface. A density profile of this type has been identified photographically with the high-temperature superconductor  $\text{YBa}_2\text{Cu}_3\text{O}_{7-x}$  (Figure 3.14). We note,

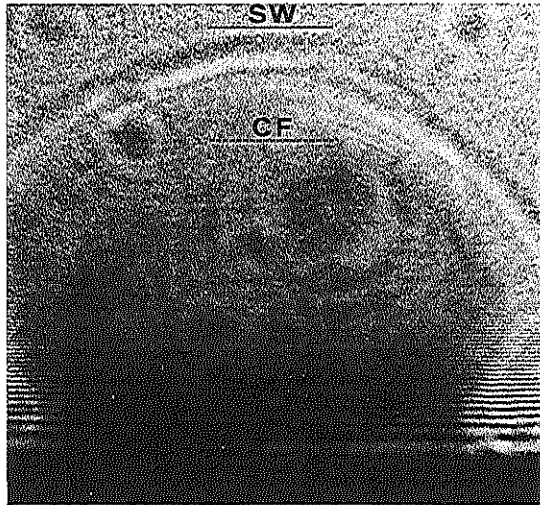


Figure 3.14.  $\text{YBa}_2\text{Cu}_3\text{O}_{7-x}$  targets with a thickness of 5 mm were exposed to a single laser pulse (248 nm, ~20 ns, diameter ~800  $\mu\text{m}$ , 1.5–2 J/cm<sup>2</sup>, normal incidence) in 0.07 atm (50 torr) of air. The released particles and shock wave were photographed by firing parallel to the target surface a second ("probe") laser pulse with a delay of 500 ns. The contact front is marked CF and the shock wave, SW. (From Kelly et al., 1992a and Gupta et al., 1991.)

however, that such photographs do not normally distinguish between reflection and recondensation.

As far as the *expansion front* is concerned, for an expansion into vacuum the relevant velocity constitutes the maximum possible value of  $u$ :

$$\hat{u} = \frac{2a_0}{\gamma - 1} \quad (3.14a)$$

For an expansion into an ambient gas, the expansion front becomes a *contact front* (*cf*) and, provided the pressure is low enough, moves in accordance with the relation

$$u_{cf} = \frac{2a_0}{\gamma - 1} \left( 1 - \frac{a_{cf}}{a_0} \right) < \hat{u} \quad (3.14b)$$

As the pressure decreases, the sound speed,  $a_{cf}$ , becomes small (due to cooling) and we retrieve  $u_{cf} = \hat{u}$ . For a high enough pressure, on the other hand, energy is expended in heating and moving the ambient gas, with the result that the contact front decelerates (Kelly and Braren, 1991; Freiwald, 1972 and 1975). A further basic change when there is an ambient gas is that a *shock wave* (*sw*) runs ahead of the *contact front* (Figure 3.14).

Equations 3.14 are not useful for analyzing data from laser-sputtering experiments, as  $T_{cf}$  (thence  $a_{cf}$ ) is difficult to measure on the relevant distance scale (0–3 mm). Far more useful is the relation between  $u_{cf}$  and the shock wave velocity  $u_{sw}$  given by

$$u_{cf} = \frac{2u_{sw}}{\gamma + 1} \left( 1 - \left( \frac{a_{am}}{u_{sw}} \right)^2 \right) \approx \frac{2u_{sw}}{\gamma + 1} \geq 0.75u_{sw} \quad (3.15)$$

where  $a_{am}$  is the sound speed in the ambient (*am*) gas. Equations 3.15 are valid for both a planar and hemispherical shock wave (Freiwald, 1972 and 1975). The origins of Eqs. 3.13–3.16 are discussed by Kelly and Braren (1991).

### 3.3.3 Effusion with Reflection

Effusion begins when, at  $t = 0$ , a photon pulse begins to strike the target surface and, as a result, particles are released from the surface for a time interval  $0 \leq t \leq \tau_r$ . In terms of Figure 3.12b the wall becomes porous at  $t = 0$ . The results for  $\gamma = \frac{5}{3}$ , expressed in terms of density versus distance, at first take the form shown by curves 0.5 and 1 in Figure 3.15. As with the outflow model,



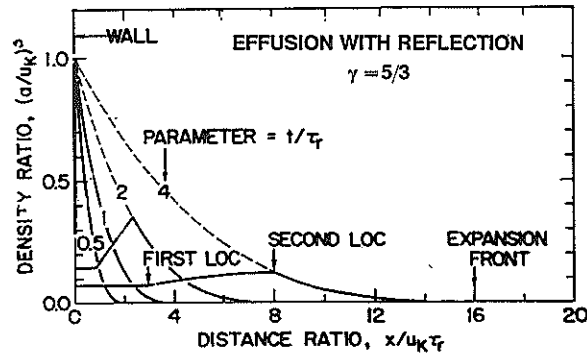


Figure 3.15. Calculated values of the density,  $\rho/\rho_K = (a/u_K)^3$ , vs. the distance,  $x/u_K\tau_r$ , for effusion with reflection. The KL, characterized for  $0 \leq t \leq \tau_r$  by  $\rho_K$  and  $u_K$ , is assumed to have zero thickness. The problem is equivalent to that of a semi-infinite reservoir of gas, as in Figure 3.12b, that is able to effuse into vacuum for  $0 \leq t \leq \tau_r$ . The indicated expansion front is that of the curve for  $t/\tau_r = 4$ .

the density decreases from an unvarying value at the target surface ("wall") to zero at the expansion front.

At  $t = \tau_r$ , the release process is assumed to cease abruptly as if the wall is resealed and, as a result, there is an abrupt change at  $x = 0$  from  $u = a = u_K$  to  $u = 0$ . That is, flow ceases at the target surface and recondensation *does not* occur. Analytical results, which have a particularly complicated form, have been obtained for  $\gamma = \frac{5}{3}$ ,  $\frac{7}{5}$ , and  $\frac{9}{7}$  (Kelly, 1992; Sibold and Urbassek, 1992; Kelly and Miotello, 1993). Those for  $\gamma = \frac{5}{3}$  are typified by curves 2 and 4 in Figure 3.15. The disturbance triggered by the abrupt fall of  $u$  at  $x = 0$  survives in the form of two LOCs. The first LOC is the result of the lower part of the disturbance at  $x = 0$  being reflected from the target surface, the second is the result of the upper part moving outward, and each corresponds to an abrupt change of slope in the density profile. The density profile therefore has three parts characterized, as a function of distance from the surface, by a low invariant value, an increase, and finally a rapid decrease to the expansion front. The particles at all times maintain contact with the surface. The sudden density decrease at  $t = \tau_r$  has been identified photographically with polymethylmethacrylate (PMMA) (Figure 3.16). Again such photographs, while they identify *effusion*, do not normally distinguish between reflection and recondensation.

As far as the expansion front is concerned, for an expansion into vacuum the relevant velocity again constitutes the maximum possible value of  $u$ . It has a form similar to Eq. 3.14a:

$$a = \frac{\gamma + 1}{\gamma - 1} u_K \quad (3.16)$$

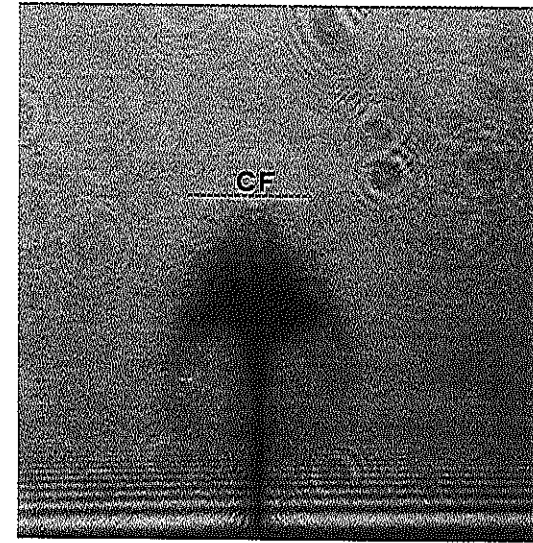


Figure 3.16. Polymethylmethacrylate (PMMA) targets with a thickness of 0.7 mm were exposed to 10 laser pulses (248 nm, ~20 ns, diameter 900  $\mu\text{m}$ , 1.34 J/cm<sup>2</sup>, normal incidence) in air. The released particles were photographed by firing parallel to the target surface a second ("probe") laser pulse with a delay of 10  $\mu\text{s}$ . The contact front is marked CF, the shock wave being beyond the field of view. (From Kelly et al., 1992a.)

For an expansion into an ambient gas, a relation with a form similar to Eq. 3.14b connects  $u_{cf}$  to  $u_K$ , while Eqs. 3.15 continue without change to connect  $u_{cf}$  to  $u_{sw}$ .

### 3.3.4 Effusion with Recondensation

Historically, the first solution obtained for effusion with recondensation was that for  $\gamma = \frac{5}{3}$ , deduced numerically by Sibold and Urbassek (1991) using the Boltzmann equation. More recently, analytical results were obtained based on the flow equations (Eqs. 3.1–3.3) and with the boundary condition at  $x = 0$  given by  $u = a = u_K$  for  $0 \leq t \leq \tau_r$ , and  $u < 0$  for  $t > \tau_r$  (Sibold and Urbassek, 1992; Kelly and Miotello, 1993). In terms of Figure 3.12c the wall becomes porous at  $t = 0$  and is resealed at  $t = \tau_r$ , a description valid also for effusion with reflection, but with the difference that particles backscattered toward the surface are now absorbed (i.e., recondensed). The results for  $\gamma = \frac{5}{3}$  closely resemble those seen in Figure 3.15, except that the density near the surface is lower and the first LOC is missing. That the density is lower is reasonable when particles can be consumed both by flow and by recondensation. The

absence of the first LOC means simply that the *lower part* of the disturbance created by the abrupt change at  $x = 0$  was not reflected from the surface.

One of the most important practical aspects of recondensation concerns the extent of recondensation: Is it a major or minor effect? A calculation has been made numerically (Miotello et al., 1992) by evaluating the recondensing quantity,  $Q$ . In fractional form,  $0 \leq Q \leq 1$ , this is just

$$Q = - \int_1^\infty \frac{u}{u_K} \left( \frac{a}{u_K} \right)^{2/(\gamma-1)} d(t/\tau_r) \quad (3.17)$$

Values are given in Table 3.10 and should be compared to  $Q = 0$  for effusion with reflection, and to an amount 0.18–0.26 associated with a KL (Table 3.8).

It is clear that it would be difficult in practice to distinguish reflection from recondensation on the basis of the density profiles. In both cases they would show a characteristic increase with distance from the surface (Figure 3.15). An interesting phenomenon is found, however, with laser-bombarded polyimide (Kelly et al., 1992b). Besides the sputtered particles expanding away from the target surface there is also prominent sideways motion, the overall expansion being three-dimensional. This was rationalized in terms of there being two groups of particles, such that the more extended group exerted a force on the less extended group and caused sideways expansion. The recondensation therefore occurs in part beyond the bombarded spot and leaves the characteristic debris pattern seen in Figure 3.17.

This in turn leads to a further observation. The symmetry of the debris normally differs from that of the bombarded spot in such a way as to imply that the flow pattern involves a rotation (Miotello et al., 1992), a similar effect being found also with deposited films (Afonso et al., 1990; Kools et al., 1992). Although the rotation may be supposed to be due to extraneous effects such as electric fields (von Gutfeld and Srinivasan, 1987) or a temperature pattern, it is in fact a simple gas-dynamic effect. To show this it is sufficient to solve the *flow equations* in two dimensions, so that Eqs. 3.1 are replaced with

TABLE 3.10 Extents of Recondensation Due to Backscattering Toward the Target Surface According to Eq. 3.17

$t/\tau_r$	Extent of Recondensation as a Fraction of the Emitted particles				
	$\gamma = \frac{5}{3}$	$\gamma = \frac{7}{5}$	$\gamma = \frac{9}{7}$	$\gamma = \frac{11}{9}$	$\gamma = 1$
1	0	0	0	0	0
2	0.024	0.040	0.048	0.048	0.070
4	0.052	0.080	0.094	0.102	0.14
8	0.072	0.110	0.13	0.14	0.19
14	0.083	0.13	0.15	0.17	0.23
20	0.089	0.14	0.17	0.18	0.26
30	0.095	0.15	0.18	0.21	0.29

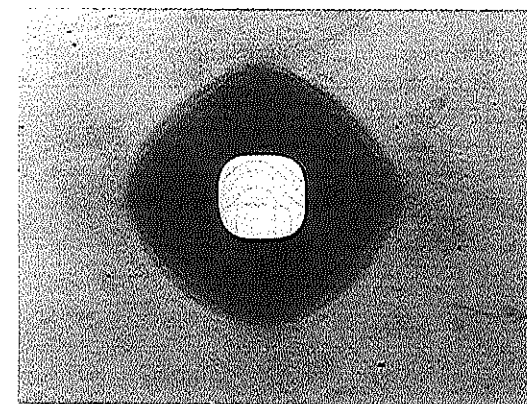


Figure 3.17. Photograph of debris on the surface of a polyimide target with a thickness of  $8 \mu\text{m}$  that has been exposed to roughly 50 laser pulses (308 nm,  $\sim 20\text{ns}$ ,  $\sim 0.25 \text{ J/cm}^2$ , normal incidence) in air. The light region near the center is a hole having a width of  $270 \mu\text{m}$  sputtered through the entire target; the dark material beyond the hole in debris due to sideways expansion of the sputtered particles. (From Miotello et al., 1992.)

$$\frac{\partial \rho}{\partial t} + \frac{\partial \rho u}{\partial x} + \frac{\partial \rho v}{\partial y} = 0 \quad (\text{continuity equation})$$

$$\frac{\partial \rho u}{\partial t} + \frac{\partial (p + \rho u^2)}{\partial x} + \frac{\partial \rho uv}{\partial y} = 0 \quad (\text{Euler equation for } u) \quad (3.18)$$

$$\frac{\partial \rho v}{\partial t} + \frac{\partial \rho uv}{\partial x} + \frac{\partial (p + \rho v^2)}{\partial y} = 0 \quad (\text{Euler equation for } v)$$

Here  $v$  is the  $y$ -direction flow velocity. The results of solving Eqs. 3.18 for a square reservoir are shown in Figure 3.18, where we recognize a remarkable similarity with Figure 3.17.

A further example which in our opinion, represents effusion with recondensation is a study in which light emitted from the etch plume of laser-bombarded Cu was studied (Pietsch et al., 1994). The crucial information was contained in the profiles of light intensity *vs.* distance.

### 3.4 FINAL COMMENTS

In pulsed laser sputtering it is necessary to distinguish between *primary* and *secondary* mechanisms. The former include the well-known collisional, thermal, electronic, exfoliation, hydrodynamic, and condensational processes. Of these processes only that termed hydrodynamic, equivalent to droplet emission as in Figure 3.9, does not have a close analog in ion sputtering (Table 3.1).

We regard the most powerful approaches for distinguishing *primary* mech-



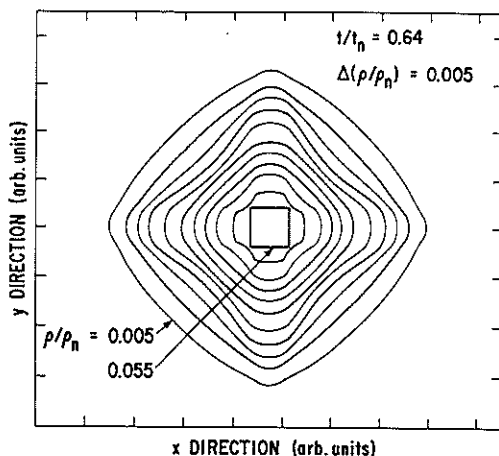


**Figure 3.18.** Density contours calculated numerically with Eqs. 3.18 for an initially square reservoir of gas that begins to expand in two dimensions when the four confining walls are removed at  $t = 0$ . The contour intervals are indicated by  $\Delta(\rho/\rho_n)$ , where  $\rho_n$  describes the reservoir at  $t = 0$ . The unitless time,  $t/t_n = 0.64$ , corresponds to the moment when the reservoir has a fraction 0.073 of the gas initially present. (From Miotello et al., 1992.)

anisms to be SEM and temperature measurement, the latter normally accomplished with TOF spectra. A crucial detail in isolating the mechanism is to appreciate that the observed rate of laser sputtering, typically 1–10 nm/pulse, can be attributed to vaporization (i.e., thermal sputtering) only if the target temperature is sufficiently high (Table 3.4), yet the inequality  $T < T_{ic}$  is respected (Table 3.5). Failing this, an electronic process is often indicated.

The *secondary* mechanisms include various types of pulsed flow processes that differ both depending on whether the release is from the surface or from a reservoir, and also depending on whether particles that are backscattered toward the surface are reflected or absorbed (i.e., recondensed) (Table 3.2). To a limited extent similar processes are found with ion sputtering, but only (as with condensed gas or organic targets) when the yield is unusually high. The flow processes cause the system to lose memory of the primary mechanism. For example, rather independently of the primary velocity distribution, a shifted Maxwellian form as in Eq. 3.11 will tend to apply. Conversely, observing a Maxwellian distribution (with or without shifting) does not necessarily indicate a thermal primary mechanism.

Often the flowing particles can be imaged photographically, and one then has the possibility of distinguishing different secondary processes. For example, the particles flowing from laser-bombarded  $\text{YBa}_2\text{Cu}_3\text{O}_{7-x}$  show a pattern like that for *outflow* (Figure 3.14), while those from laser-bombarded polymethylmethacrylate show a pattern more nearly like that for *effusion* (Figure 3.16).

These photographs do not normally distinguish between reflection and recondensation. The relevance of recondensation is, however, demonstrated in those instances where there is sideways expansion and debris therefore extend beyond the bombarded spot (Figure 3.17). It has, in our opinion, also been demonstrated for laser-bombarded Cu (Pietsch et al., 1994).

## REFERENCES

- Afonso, C. N., R. Serna, F. Catalina, and D. Bermejo (1990), *Appl. Surf. Sci.* **46**, 249.
- Akhsakhalyan, A. D., Yu. A. Bityurin, S. V. Gaponov, A. A. Gudkov, and V. I. Luchin (1982a), *Sov. Phys. Tech. Phys.* **27**, 969.
- Akhsakhalyan, A. D., Yu. A. Bityurin, S. V. Gaponov, A. A. Gudkov, and V. I. Luchin (1982b), *Sov. Phys. Tech. Phys.* **27**, 973.
- Auciello, O., and R. Kelly (1982), *Radiat. Eff.* **66**, 195.
- Batanov, V. A., and V. B. Fedorov (1973), *JETP Lett.* **17**, 247.
- Braren, B., K. G. Casey, and R. Kelly (1991), *Nucl. Instrum. Meth.* **B58**, 463.
- Braun, M., J. L. Whitton, and B. Emmoth (1979), *J. Nucl. Mat.* **85/86**, 1091.
- Brown, W. L., M. F. Jarrold, R. L. McEachern, M. Sosnowski, G. Takaoka, H. Usui, and I. Yamada (1991), *Nucl. Instrum. Meth.* **B59/60**, 182.
- Cercignani, C. (1981), in *Rarefied Gas Dynamics*, vol. I, S. S. Fisher, ed., AIAA, New York, p. 305.
- Chase, M. W., C. A. Davies, J. R. Downey, D. J. Frurip, R. A. McDonald, and A. N. Syverud (1986), *JANAF Thermochemical Tables*, 3d ed. American Chemical Society, New York.
- Chen, L. F., and K. S. Song, *Nucl. Instrum. Meth. B* (in press).
- Donà-dalle Rose, L. F., A. Miotello, and R. Brotto (1983), *Radiat. Eff.* **69**, 1.
- Dreyfus, R. W., R. Kelly, and R. E. Walkup (1987), *Nucl. Instrum. Meth.* **B23**, 557.
- Dreyfus, R. W., R. E. Walkup, and R. Kelly (1986), *Radiat. Eff.* **99**, 199.
- Fleischer, R. L., P. B. Price, and R. M. Walker (1965), *J. Appl. Phys.* **36**, 3645.
- Follstaedt, D. M., S. T. Picraux, P. S. Peercy, and W. R. Wampler (1981), *Appl. Phys. Lett.* **39**, 327.
- Freiwald, D. A. (1972), *J. Appl. Phys.* **43**, 2224.
- Freiwald, D. A., and R. A. Axford (1975), *J. Appl. Phys.* **46**, 1171.
- Gaponov, S. V., B. M. Luskun, B. A. Nesterov, and N. N. Salashchenko (1977), *Sov. Phys. Solid State* **19**, 1736.
- Garrison, B. J., and R. Srinivasan (1985), *J. Appl. Phys.* **57**, 2909.
- Gupta, A., B. Braren, K. G. Casey, B. W. Hussey, and R. Kelly (1991), *Appl. Phys. Lett.* **59**, 1302.
- Haglund, R. F., and R. Kelly (1993), *Kgl. Danske Vid. Selsk. Mat. Fys. Medd.* **43**, 527.
- Helvajian, H., and R. Welle (1989), *J. Chem. Phys.* **91**, 2616.
- Hoheisel, W., M. Vollmer, and F. Träger (1991), *Laser Ablation: Mechanisms and Applications*. Springer-Verlag, Berlin, p. 77.
- Itoh, N., and T. Nakayama (1982), *Phys. Lett.* **92A**, 471.

- Jodeh, S., J. Villanueva, S. Deshmukh, and G. P. Reck (in press), *J. Phys. Chem.*
- Jöst, B., B. Schueler, and F. R. Krueger (1982), *Z. Nat. Forsch.* **37a**, 18.
- Kelly, R. (1984a), *Rad. Effects* **80**, 273.
- Kelly, R. (1984b), in *Ion Bombardment Modification of Surfaces: Fundamentals and Applications*, (O. Auciello and R. Kelly, eds.), Elsevier, Amsterdam, p. 27.
- Kelly, R. (1990a), *Nucl. Instrum. Meth.* **B46**, 441.
- Kelly, R. (1990b), *J. Chem. Phys.* **92**, 5047.
- Kelly, R. (1992), *Phys. Rev.* **A46**, 860.
- Kelly, R., and B. Braren (1991), *Appl. Phys.* **B53**, 160.
- Kelly, R., and R. W. Dreyfus (1988a), *Surf. Sci.* **198**, 263.
- Kelly, R., and R. W. Dreyfus (1988b), *Nucl. Instrum. Meth.* **B32**, 341.
- Kelly, R., and A. Miotello (1993), *Appl. Phys.*, **B57**, 145.
- Kelly, R., and J. E. Rothenberg (1985), *Nucl. Instrum. Meth.* **B718**, 755.
- Kelly, R., J. J. Cuomo, P. A. Leary, J. E. Rothenberg, B. E. Braren, and C. F. Aliotta (1985), *Nucl. Instrum. Meth.* **B9**, 329.
- Kelly, R., A. Miotello, B. Braren, A. Gupta, and K. Casey (1992a), *Nucl. Instrum. Meth.* **B65**, 187.
- Kelly, R., A. Miotello, B. Braren, and C. E. Otis (1992b), *Appl. Phys. Lett.* **60**, 2980.
- Kissel, J., and F. R. Krueger (1987), *Appl. Phys.* **A42**, 69.
- Knight, C. J. (1982), *AIAA J.* **20**, 950.
- Kools, J. C. S., T. S. Baller, S. T. de Zwart, and J. Dieleman (1992), *J. Appl. Phys.* **71**, 4547.
- Leismann, P., V. Henc-Bartolic, U. Rebhan, and H. J. Kunze (1984), *Phys. Scr.* **30**, 186.
- Liu, J. M., L. A. Lompre, H. Kurz, and N. Bloembergen (1984), *Appl. Phys.* **A34**, 25.
- Liu, J. M., R. Yen, H. Kurz, and N. Bloembergen (1981), *Appl. Phys. Lett.* **39**, 755.
- McClelland, G. M., K. L. Saenger, J. J. Valentini, and D. R. Herschbach (1979), *J. Phys. Chem.* **83**, 947.
- Miotello, A., R. Kelly, B. Braren, and C. E. Otis (1992), *Appl. Phys. Lett.* **61**, 2784.
- Nakai, Y., K. Hattori, A. Okano, N. Itoh, and R. F. Haglund (1991) *Nucl. Instr. Meth.* **B58**, 452.
- Nakata, T., M. Kakehata, and F. Kannari (in press), *J. Phys. D.*
- Namiki, A., T. Kawai, and K. Ichige (1986), *Surf. Sci.* **166**, 129.
- NoorBatcha, I., R. R. Lucchese, and Y. Zeiri (1987), *J. Chem. Phys.* **86**, 5816.
- NoorBatcha, I., R. R. Lucchese, and Y. Zeiri (1988), *J. Chem. Phys.* **89**, 5251.
- Novis, Y., J. J. Pireaux, A. Brezini, E. Petit, R. Caudano, P. Lutgen, G. Feyder and S. Lazare (1988), *J. Appl. Phys.* **64**, 365.
- Otis, C. E., and P. M. Goodwin (1993), *J. Appl. Phys.*, **73**, 1957
- Pietsh, W., B. Dubreuil, and A. Briand (in press), *Appl. Phys. B.*
- Reif, F. (1965), *Fundamentals of Statistical and Thermal Physics*, McGraw-Hill Kogakusha, Tokyo.
- Rothenberg, J. E., and R. Kelly (1984), *Nucl. Instrum. Meth.* **B1**, 291.
- Saenger, K. L. (1981), *J. Chem. Phys.* **75**, 2467.
- Saenger, K. L. (1991), *J. Appl. Phys.* **70**, 5629.

- Saenger, K. L., Chapter 7 of this book, tables 1 and 2.
- Sibold, D., and H. M. Urbassek (1991), *Phys. Rev.* **A43**, 6722.
- Sibold, D., and H. M. Urbassek (1992), *Phys. Fluids* **A4**, 165.
- Srinivasan, R., B. Braren, and R. W. Dreyfus (1987), *J. Appl. Phys.* **61**, 372.
- Stanyukovich, K. P. (1960), *Unsteady Motion of Continuous Media*, Pergamon, London, pp. 121, 147, 151, 170.
- Touloukian, Y. S., R. K. Kirby, R. E. Taylor, and P. D. Desai (1975), *Thermal Expansion, Metallic Elements and Alloys, Thermophysical Properties of Matter*, Vol. 12, IFI/Plenum, New York.
- Urbassek, H. M., and J. Michl (1987), *Nucl. Instrum. Meth.* **B22**, 480.
- Urbassek, H. M., and D. Sibold (1993), *Phys. Rev. Lett.*, **70**, 1886.
- Venkatesan, T., X. D. Wu, A. Inam, and J. B. Wachtman (1988), *Appl. Phys. Lett.* **52**, 1193.
- Vertes, A., P. Juhasz, M. de Wolf, and R. Gijbels (1989a), *Int. J. Mass. Spect. Ion Proc.* **94**, 63.
- Vertes, A., P. Juhasz, L. Balazs, and R. Gijbels (1989), in *Microbeam Analysis-1989b*, (P. E. Russell, ed.), San Francisco Press, San Francisco, p. 273.
- von Gutfeld, R. J., and R. Srinivasan (1987), *Appl. Phys. Lett.* **51**, 15.
- Wautelet, M., and L. D. Laude (1980), *Appl. Phys. Lett.* **36**, 197.
- Wien, K. (1992), *Nucl. Instrum. Meth.* **B65**, 149.
- Ytrehus, T. (1977), in *Rarefied Gas Dynamics*, vol. II, (J. L. Potter, ed.) AIAA, New York, p. 1197.